

REPORT DOCUMENTATION PAGEForm Approved
OMB NO. 0704-0188

Public Reporting burden for this collection of information is estimated to average 1 hour per response, including the time for reviewing instructions, searching existing data sources, gathering and maintaining the data needed, and completing and reviewing the collection of information. Send comment regarding this burden estimate or any other aspect of this collection of information, including suggestions for reducing this burden, to Washington Headquarters Services, Directorate for Information Operations and Reports, 1215 Jefferson Davis Highway, Suite 1204, Arlington, VA 22202-4302, and to the Office of Management and Budget, Paperwork Reduction Project (0704-0188), Washington, DC 20503.

1. AGENCY USE ONLY (Leave Blank)		2. REPORT DATE 6/8/04	3. REPORT TYPE AND DATES COVERED Final Report 91/99 to 3/31/03	
4. TITLE AND SUBTITLE "Fermi Electronics: A Means of Correlating and Canceling Shot Noise from Solid State Devices"			5. FUNDING NUMBERS DAAD19-99-1-0296	
6. AUTHOR(S) Brown, Elliott R.				
7. PERFORMING ORGANIZATION NAME(S) AND ADDRESS(ES) Regent of the University of California 10920 Wilshire Blvd. 12th fl Los Angeles, CA 90024			8. PERFORMING ORGANIZATION REPORT NUMBER	
9. SPONSORING / MONITORING AGENCY NAME(S) AND ADDRESS(ES) U. S. Army Research Office P.O. Box 12211 Research Triangle Park, NC 27709-2211			10. SPONSORING / MONITORING AGENCY REPORT NUMBER 40135.1-EL	
11. SUPPLEMENTARY NOTES The views, opinions and/or findings contained in this report are those of the author(s) and should not be construed as an official Department of the Army position, policy or decision, unless so designated by other documentation.				
12 a. DISTRIBUTION / AVAILABILITY STATEMENT Approved for public release; distribution unlimited.			12 b. DISTRIBUTION CODE	
13. ABSTRACT (Maximum 200 words) This project has developed a formalism for computing the shot noise in resonant-tunneling structures having an arbitrary number of quantum wells. It is based on the electrostatic feedback effect in quantum-well structures and is the first known shot noise formalism that treats the electrostatic and quantum effects in a self-consistent fashion. Simulation results are analyzed and compared to experimental results for an InGaAs/AlAs double-barrier structure, which is the fastest resonant tunneling diode ever characterized for its noise properties. Shot noise reduction and enhancement are predicted in the positive and negative differential resistance region, respectively, in satisfactory agreement with experiment. The shot noise reduction effect is then studied for multiple-well resonant tunneling diodes. It is found that in properly designed structures the shot noise factor				
14. SUBJECT TERMS thermal noise, shot noise, resonant tunnelling devices, quantum-well structures			15. NUMBER OF PAGES 45	
			16. PRICE CODE	
17. SECURITY CLASSIFICATION OR REPORT UNCLASSIFIED	18. SECURITY CLASSIFICATION ON THIS PAGE UNCLASSIFIED	19. SECURITY CLASSIFICATION OF ABSTRACT UNCLASSIFIED	20. LIMITATION OF ABSTRACT UL	

NSN 7540-01-280-5500

Standard Form 298 (Rev.2-89)
Prescribed by ANSI Std. Z39-18
298-102

Enclosure 1

20040709 057

BEST AVAILABLE COPY

REPORT DOCUMENTATION PAGE (SF298)
(Continuation Sheet)

decreases significantly with well number up to at least three, and that this decrease can occur without sacrificing much of the current density or speed of the devices. The minimum room-temperature shot noise factor predicted by this work is 0.24 in a triple-well structure.

This project has also paved the way for a new type of "Fermi-electronic" device – the resonant-plasmon-mediated switch. In this type of device, the quantum well of a resonant tunneling devices would be replaced by a semiconducting matrix filled with a 3D distribution of semimetallic nanoparticles. Each nanoparticle is capable of storing charge and, therefore, in providing electrostatic feedback to free carriers. Because the nanoparticles are not directly in the path of the charge carriers, it would be possible to get the noise suppression of resonant-tunnel diodes but over a much broader range of voltage and at much higher current densities. This type of mechanism should be capable of smoothing out thermal, or Johnson-Nyquist noise, when the device is biased out of thermodynamic equilibrium.

As a first test of resonant plasmon-mediated structures, near-infrared attenuation measurements were made between $\lambda = 0.5 \mu\text{m}$ ($h\nu = 2.48 \text{ eV}$) and $10.0 \mu\text{m}$ ($h\nu = 0.124 \text{ eV}$) on three GaAs epitaxial layers containing thin ErAs layers. At wavelengths in the vicinity of $2.5 \mu\text{m}$ well below the GaAs band edge, an asymmetric resonant attenuation signature was observed that increases in strength monotonically with the ErAs nanoparticle density. The peak attenuation coefficient was found to be 1300, 1850, and 2380 cm^{-1} for ErAs volumetric fractions of 0.56, 0.85, and 1.13 %, respectively. The attenuation signature is fit well by a Maxwell-Garnett composite-dielectric model that treats the ErAs as semimetallic spherical particles having carrier concentrations and the corresponding effective masses in accordance with separate band-structure computations. The resulting absorption peak corresponds to the fundamental-mode surface-plasmon (i.e., Frohlich) resonance of the ErAs nanoparticles embedded in GaAs.



**University of California, Los Angeles
The Henry Samueli School of Engineering
Department of Electrical Engineering**

Final Report

**Fermi Electronics: A Means of
Correlating and Canceling Shot Noise
from Solid State Devices**

**Army Research Office
Award # DAAD19-99-1-0296**

Submitted by: Prof. Elliott R. Brown

June 8, 2004

FERMI ELECTRONICS: A MEANS OF CORRELATING AND CANCELING
SHOT NOISE FROM SOLID STATE DEVICES

Final Report for research supported by the U.S. Army Research Office

Grant Number: DAAD19-99-1-0296

Table of Contents

Abstract	2
1. Introduction	2
2. Noise suppression in resonant tunneling devices	5
2.1 Fabrication procedure	5
2.2 Modeling of current-voltage characteristics of RTDs	6
2.2.1 Material parameters and energy-band structure	7
2.2.2 Computation of the charge and current density	9
2.2.3 Computational method	14
2.3 Noise mechanisms in RTDs	17
2.3.1 Thermal noise	18
2.3.2 Shot noise	18
2.4 Modeling of shot noise in RTDs	19
2.4.1 Analytic modeling	19
2.4.2 Numerical modeling	21
2.4.3 Interpretation of experimental data	23
2.4.4 Comparison of numerical model and experiment	25
2.5 Simulation of shot noise in multiple-well RTDs	27
2.5.1 InGaAs/AlAs Structures	27
2.5.2 InGaAs/InP Structures	31
2.6 Promising application	32
3. Resonant-Plasmon-Mediated Nanostructures	33
3.1 Optical Characterization of ErAs:GaAs	34
3.2 Modeling of ErAs Nanoparticles: Surface Plasmons	36
3.3 Surface Plasmon Effect on Optical Transmission	38
Conclusion	41
References	41
Listing of Publications and Technical Reports	44
Listing of Scientific Personnel Earning Advanced Degrees	45

Abstract

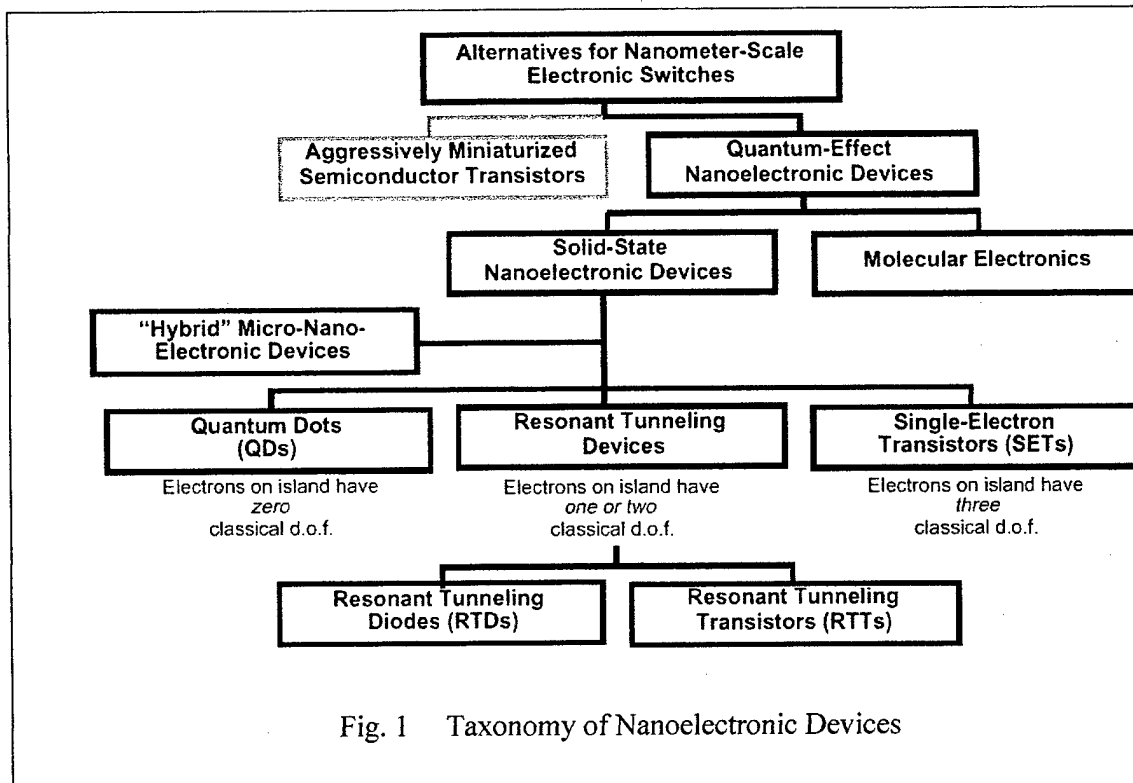
This project has developed a formalism for computing the shot noise in resonant-tunneling structures having an arbitrary number of quantum wells. It is based on the electrostatic feedback effect in quantum-well structures and is the first known shot noise formalism that treats the electrostatic and quantum effects in a self-consistent fashion. Simulation results are analyzed and compared to experimental results for an InGaAs/AlAs double-barrier structure, which is the fastest resonant tunneling diode ever characterized for its noise properties. Shot noise reduction and enhancements are predicted in the positive and negative differential resistance region, respectively, in satisfactory agreement with experiment. The shot noise reduction effect is then studied for multiple-well resonant tunneling diodes. It is found that in properly designed structures the shot noise factor decreases significantly with well number up to at least three, and that this decrease can occur without sacrificing much of the current density or speed of the devices. The minimum room temperature shot noise factor predicted by this work is 0.24 in a triple-well structure.

This project has also paved the way for a new type of "Fermi-electronic" device – the resonant-plasmon-mediated switch. In this type of device, the quantum well of a resonant tunneling devices would be replaced by a semiconducting matrix filled with a 3D distribution of semimetallic nanoparticles. Each nanoparticle is capable of storing charge and, therefore, in providing electrostatic feedback to free carriers. Because the nanoparticles are not directly in the path of the charge carriers, it would be possible to get the noise suppression of resonant-tunnel diodes but over a much broader range of voltage and at much higher current densities. This type of mechanism should be capable of smoothing out thermal, or Johnson-Nyquist noise, when the device is biased out of thermodynamic equilibrium.

As a first test of resonant plasmon-mediated structures, near-infrared attenuation measurements were made between $\lambda = 0.5 \mu\text{m}$ ($h\nu = 2.48 \text{ eV}$) and $10.0 \mu\text{m}$ ($h\nu = 0.124 \text{ eV}$) on three GaAs epitaxial layers containing thin ErAs layers. At wavelengths in the vicinity of $2.5 \mu\text{m}$ well below the GaAs band-edge, an asymmetric resonant attenuation signature was observed that increases in strength monotonically with the ErAs nanoparticle density. The peak attenuation coefficient was found to be 1300, 1850, and 2380 cm^{-1} for ErAs volumetric fractions of 0.56, 0.85, and 1.13 %, respectively. The attenuation signature is fit well by a Maxwell-Garnett composite-dielectric model that treats the ErAs as semimetallic spherical particles having carrier concentrations and the corresponding effective masses in accordance with separate band-structure computations. The resulting absorption peak corresponds to the fundamental-mode surface-plasmon (i.e., Frohlich) resonance of the ErAs nanoparticles embedded in GaAs.

1. Introduction

For the past forty years, electronic computers have grown more powerful as their basic sub-unit, the transistor, has shrunk. However, the laws of quantum mechanics plus the limitations of materials and fabrication techniques soon are likely to inhibit further improvement in the performance with reduction in the size of today's bulk-effect semiconductor transistors. Researchers have projected that as the overall size of the bulk-effect semiconductor transistor is miniaturized to approximately 0.1 micron and below, the devices may not improve significantly. Thus, in order to continue the miniaturization of integrated circuits well into the next century, it is likely that present-day micron-scale

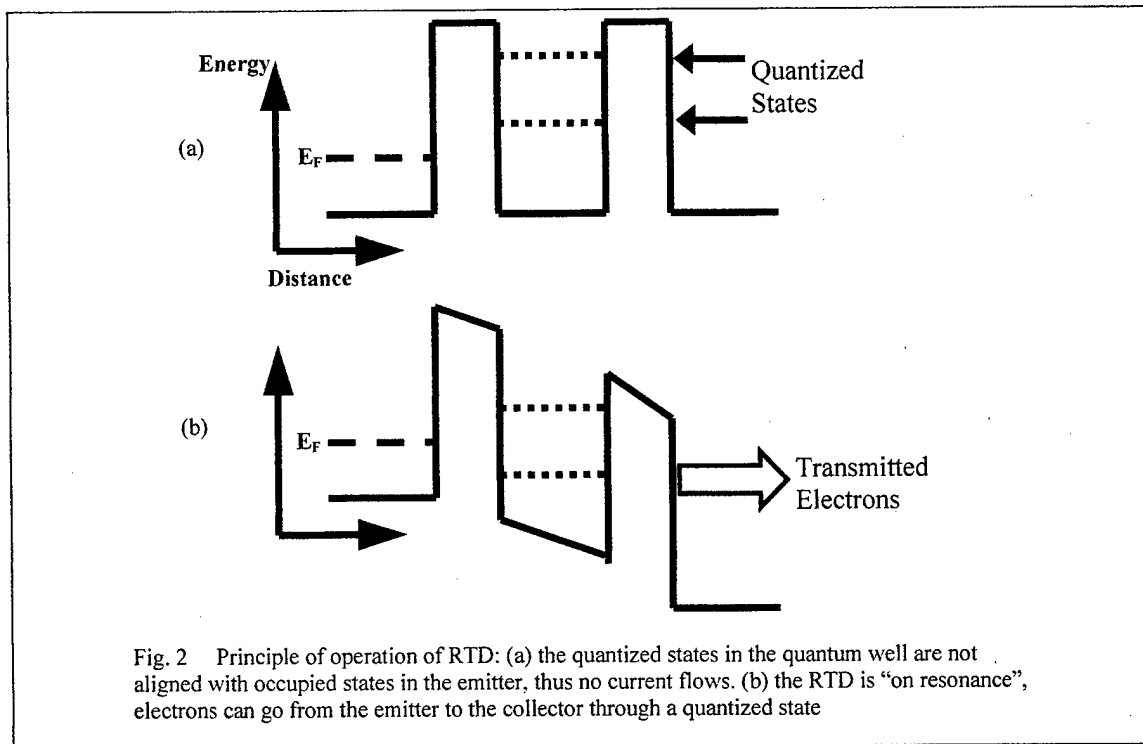


device designs will be replaced with new designs or new device types that take advantage of the quantum mechanical effects that dominate on the much smaller, nanometer scale. Quantum-effect nanoelectronic devices are a promising alternative for continuing to increase the density and speed of integrated circuits.

Among the numerous nanoelectronic approaches proposed (Fig. 1) and demonstrated, resonant tunneling are a strong candidate for circuit applications due to their negative differential resistance (NDR) characteristics, structural simplicity, relative ease of fabrication, inherent high speed, flexible design, and versatile circuit functionality. There are also good practical reasons to believe that the resonant tunneling diode (RTD) may be the next device based on quantum-confined heterostructures to make the transition from the world of research into practical application. Progress in epitaxial growth has improved the peak-to-valley current ratio at room temperature even beyond that required for many circuit applications. This is what distinguishes the RTD from other interesting quantum device concepts that show weak, if any, desired phenomena at room temperature.

Moreover the study of resonant tunneling diodes provides valuable knowledge of the quantum aspects of electron transport in mesoscopic systems. Tunneling current is becoming a more interesting issue in today's transistors. Quantization of carriers in one, two or three dimensions is a promising basis of device design in the future. The focus of the present work is the noise characteristics of resonant tunneling diodes.

As semiconductor devices have shrunk in size, the intrinsic noise is more than ever a limiting factor of their capabilities, especially in nanoelectronic devices. Given a specific device type, the traditional approach to noise control and suppression has occurred at the circuit level where a large number of techniques (e.g. negative feedback) have been developed to achieve low-noise circuits with garden-variety devices. The present work is aimed at engineering noise suppression in the semiconductor device



itself, utilizing the quantum properties of nanostructures. Two fundamental noise mechanisms that must be considered on the nanoscale are thermal noise and shot noise.

Shot noise is associated with the fluctuations of emission times of carriers across a limiting barrier in any electronic device. This type of noise is the dominant source of noise in bipolar transistors, p-n diodes and hetero-barrier diodes. The power spectral density of such shot noise is given by $S_I = 2e\gamma I$, where I is the average current, e is the magnitude of the electronic charge, and γ the shot noise factor [1]. For $\gamma = 1.0$, the phenomenon is statistically Poissonian and called full shot noise. However significant deviations from the full shot noise occur in double-barrier resonant tunneling diodes (RTDs). Shot noise reduction as low as $\gamma = 0.35$ [2] at 77 K has been measured, generating interest in using resonant-tunneling structures for their low-noise characteristics.

This research features the first shot noise calculation for multiple (>2) quantum well resonant tunneling structures that includes electrostatic-feedback and self-consistent coupling between Schrödinger and Poisson equations. It will support the claim that shot noise reduction effect is caused by the electrostatic repulsion endured by injected carriers due to the charge stored in the quantum well(s). The thesis is organized as follows. The second section presents the operating principles and fabrication processes of RTDs. The third section develops in detail the methodology enabling the simulation of the current-voltage characteristics of resonant tunneling diodes from fundamental principles. Fluctuations around the average values, and particularly shot noise, are studied in the fourth section. In the fifth section the simulation results are analyzed and compared to experimental results for an InGaAs/AlAs single-well RTD. Subsequently the shot noise reduction effect is studied for multiple-well (up to 4) RTDs, suggesting that properly designed multiple-well RTDs will display even lower shot noise properties than single-well devices. In the final section the use of multiple-well RTDs for low-noise application is envisioned.

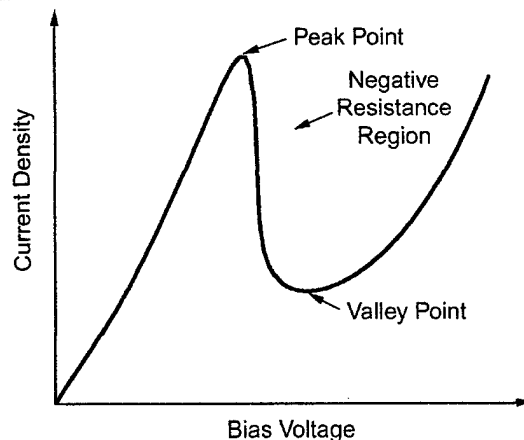


Fig. 3 Typical I-V curve of a double-barrier RTD

2. Noise suppression in resonant tunneling devices

Resonant tunneling diodes are fabricated from layers of two different III/V semiconductor alloys, such as the pair $\text{In}_{0.53}\text{Ga}_{0.47}\text{As}/\text{AlAs}$. A double-barrier resonant tunneling diode is made by embedding two layers of the material with the larger band gap (AlAs) within layers of the other material (InGaAs), creating a quasibound potential well where electrons can reside. RTDs are made with wells typically 4 to 6 nanometers in width. Whenever electrons are confined between two such closely spaced barriers, quantum mechanics restricts their energies to one of a discrete set of quantized levels. The only way for electrons to pass through the device is to "tunnel," quantum mechanically, through the two barriers. The probability that the electrons can tunnel is dependent on their energy relative to the discrete levels in the well of the device. As illustrated in Fig. 2(a), if the energy of the incoming electron differs from the levels allowed inside the potential well, then current does not flow. However, when the energy of the incoming electron aligns with one of the levels, as shown in Fig. 2(b), the electron is said to be "in resonance" with the well and current flows through the device.

The resulting current-voltage curve (Fig.3) features a negative differential resistance region at room temperature, making the RTD a practical active device. P-N (Esaki) tunnel diodes, which display the same kind of characteristics, are used commercially in microwave oscillators, mixers, detectors, and multipliers. RTDs are displacing Esaki diodes in some of these applications because of their superior speed.

2.1. Fabrication Procedure

The most critical part of the fabrication procedure for resonant tunneling diodes is the growth of the wafer. The peak current density of RTDs is inverse-exponentially proportional to the width of the barriers. So the thickness of the grown barriers must be carefully monitored (using techniques such as reflection high energy electron diffraction or RHEED that provide feedback during epitaxial growth) in monolayer accuracy. Other requirements are to avoid the diffusion of the dopants into the barriers, to smooth the heterointerface between the two materials, and to accommodate the residual stress

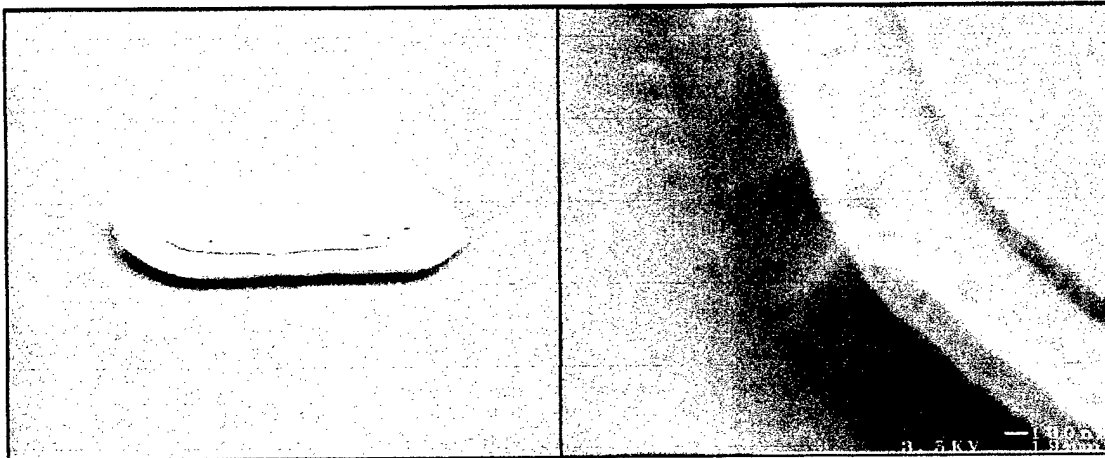


Fig. 4 Left: mesa defining the RTD – Right: zoom on the under-etch due to RIE

between the two semiconductor alloys (for example the material pair $\text{In}_{0.53}\text{Ga}_{0.47}\text{As}/\text{AlAs}$ exhibits a 3.5% lattice mismatch).

Once the RTD wafer is grown, fabrication of diodes can be achieved via a simple one-mask process. Grids of ohmic metal (e.g. Ni/Ge/Au) top contacts are defined by a standard photolithographic liftoff. The metal contacts are then used to mask the sample during the etching step (e.g. reactive ion etching with CCl_2F_2), creating mesa devices (Fig. 4). The etching process is stopped about 100 nm below the bottom barrier of the RTD. The second ohmic contact is made on the backside of the wafer or around the mesa. If probing is too tricky due to the small size of contacts or if the devices need to be packaged for RF measurements, additional steps are required. First, a dielectric deposition must be made by PECVD to fill the volume around and on top of the mesas, and then RIE is used to etch openings on top of the mesas. Finally metal is deposited and patterned to define large landing pads.

2.2 Modeling of current-voltage characteristics of RTDs

Various formalisms of quantum transport in resonant tunneling diodes have been developed over the years [3]. In this work the goal was not to develop an exhaustive model taking every physical effect into account, but rather to develop a framework suitable for the study of noise properties in structures with thin barriers. In such structures the electron transport is largely ballistic, which simplifies the analysis significantly. From a first-principles point of view, the RTD is an open quantum system in which electron transport is three dimensional, time dependent, time irreversible, dissipative, and many-body interactive. Both particle and energy exchanges occur frequently with the outlying semiconductor material. The device is therefore very different from a simple isolated quantum system, where a conservative Hamiltonian and the boundary conditions for the Schrödinger equation may be readily formulated. On the other hand, a full many-body formalism may not be necessary for calculations of specific device properties since approximations and simplifications can be used, provided that the major transport processes can be properly modeled.

100 nm $\text{In}_{0.53}\text{Ga}_{0.47}\text{As}$ $N_D=1.3 \times 10^{19} \text{ cm}^{-3}$
100 nm $\text{In}_{0.53}\text{Ga}_{0.47}\text{As}$ $N_D=2.0 \times 10^{18} \text{ cm}^{-3}$
5 nm $\text{In}_{0.53}\text{Ga}_{0.47}\text{As}$ $N_D=2.0 \times 10^{16} \text{ cm}^{-3}$
1.4 nm AlAs UNDOPED
6.1 nm $\text{In}_{0.53}\text{Ga}_{0.47}\text{As}$ UNDOPED
1.4 nm AlAs UNDOPED
75 nm $\text{In}_{0.53}\text{Ga}_{0.47}\text{As}$ $N_D=1.0 \times 10^{17} \text{ cm}^{-3}$
200 nm $\text{In}_{0.53}\text{Ga}_{0.47}\text{As}$ $N_D=2.0 \times 10^{18} \text{ cm}^{-3}$
200 nm $\text{In}_{0.53}\text{Ga}_{0.47}\text{As}$ $N_D=1.3 \times 10^{19} \text{ cm}^{-3}$
N^+ InP SUBSTRATE

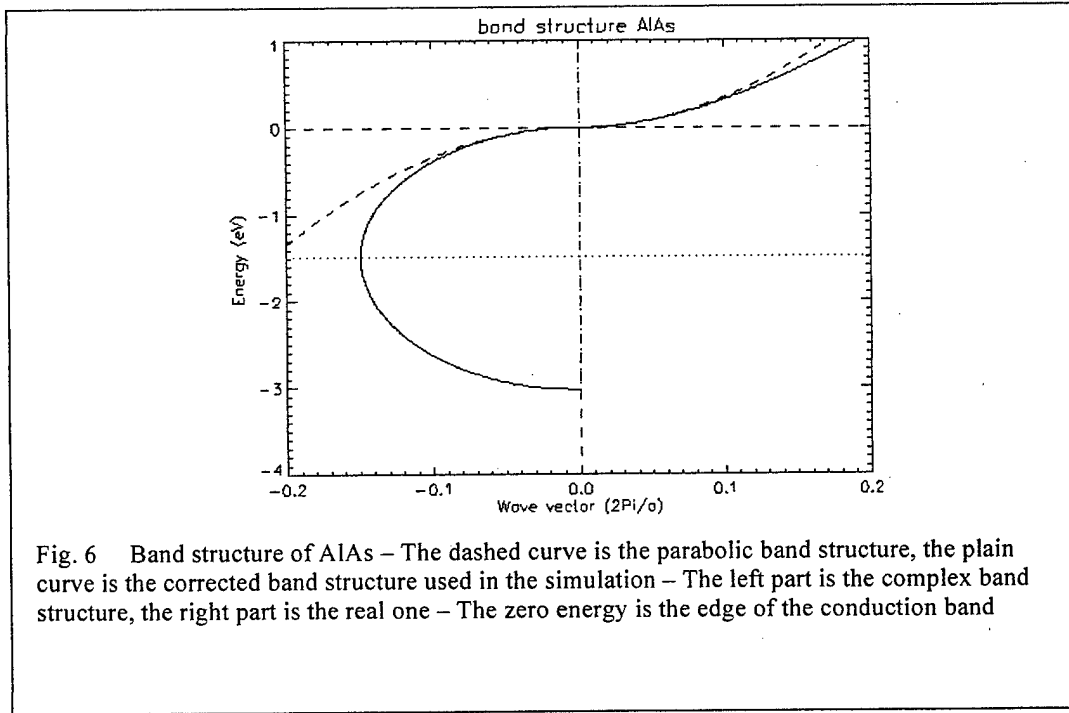
Fig. 5 Epitaxial-layer profile of the test structure

The model used in this work is based on the envelope function description of electron states. Since quantum phenomena must be included, the effective mass Schrödinger equation is invoked to calculate the electron wave function, neglecting the rapidly varying periodic component. The primary underlying assumption is that the transport is coherent, meaning that there is conservation of the transverse crystal momentum of the tunneling carriers and that phase-breaking processes are neglected in the quantum-well(s) region. This assumption remains reasonable as long as the length of the tunneling region, and especially the thickness of the barriers, is negligible in comparison with the mean free path of electrons under thermal excitation, which is the case for the structures studied in this work.

All through this section, the presentation of the modeling will be illustrated by a realistic test structure whose epitaxial-layer profile is shown in Fig. 5. A few remarks can be made about the design of this structure. As in every RTD, both ends of the device are heavily doped to obtain the least resistive ohmic contact as possible. The AlAs barrier layers and the $\text{In}_{0.53}\text{Ga}_{0.47}\text{As}$ quantum well are undoped and surrounded by lowly doped buffer layers to preserve the purity and the quality of the barriers and heterointerfaces. The buffer layer on the emitter side is made short to obtain a high peak current density. The collector buffer layer is made long because the capacitance of the device decreases with the thickness of this layer [6], making the device faster. Oscillations up to 200 GHz have been obtained with this structure [4].

2.2.1 Material parameters and energy-band structure

Accurate material and energy-band parameters are required to be able to simulate quantitatively any nanostructure. For example, because the peak current density of a RTD is exponentially proportional to the width of the barriers, a good knowledge of the lattice constant is important because the width of the barriers is necessarily a multiple of the monolayer length of the material. The $\text{In}_{0.53}\text{Ga}_{0.47}\text{As}/\text{AlAs}$ material system presents an additional difficulty because these materials are not lattice-matched. Because the AlAs barriers are very thin, it is assumed that all the stress due to the 3.5% lattice mismatch is endured by AlAs [5]. Because $\text{In}_{0.53}\text{Ga}_{0.47}\text{As}$ has a larger lattice constant, the lateral stress



is tensional. Thus by Hooke's law, the longitudinal stress is compressive. It follows that the AlAs band gap is reduced along with its longitudinal lattice constant and conduction-band offset. The parameter values used in the simulation are listed in Appendix 1.

In this work, only electron tunneling through the Γ valley is considered, consistent with the fact that intersubband scattering is neglected. This is perhaps the most critical simplification in comparison with more rigorous models, but it is also what makes our model elegant and easy on computer resources. This is often called the single-band model since only Γ -point conduction-band component of the envelope function is used in the tunneling computations. The Γ -point valence-band components are assumed to be negligible.

Using a single-band model, the introduction of the non-parabolicity in the band structure is critical to obtaining a good agreement with experiments (Fig. 6). The conduction band offset for $\text{In}_{0.53}\text{Ga}_{0.47}\text{As}/\text{AlAs}$ heterostructures is estimated at 1.2 eV. So the tunneling of electrons through the AlAs barriers happens very deep below the AlAs conduction band edge. A parabolic imaginary band structure will have the effect of strongly underestimating the current density through the device [7]. So the parabolic dispersion relationship is generalized to an imaginary band structure that connects the conduction band and the light-hole valence band [8]:

$$E = E_c - \frac{\hbar^2 \eta^2}{m^*} \left(1 \pm \sqrt{1 + \frac{k^2}{\eta^2}} \right) \quad \text{with} \quad \eta = \sqrt{\frac{E_g}{\hbar^2 \left(\frac{1}{m^*} + \frac{1}{m_{lh}} \right)}}$$

In the material composing the quantum well, non-parabolicity is also important because it has a great impact on the calculated position of the energy levels in the quantum well. Non-parabolicity is introduced via an energy dependent effective mass [9]:

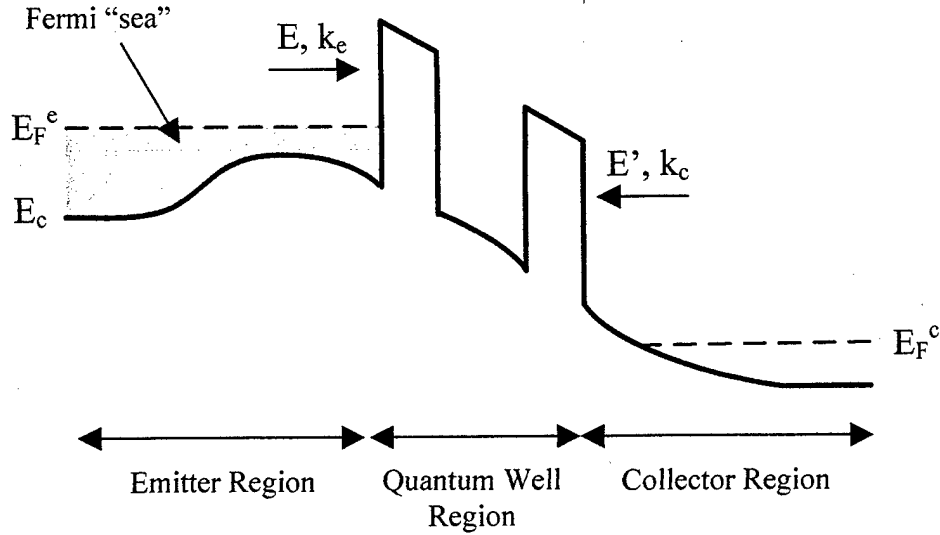


Fig. 7 Typical potential profile of a double-barrier RTD under bias

$$m^*(E) = m^*(0)(1 + \alpha E) \quad \text{with} \quad \alpha = \left(1 - \frac{m^*(0)}{m_o}\right)^2 E_g^{-1}$$

where m_o is the vacuum mass of an electron and E_g is the gap energy. These corrections to the parabolic dispersion relationship allow one to avoid the use of a multi-band tight-binding model, and appear to be accurate enough to simulate the main physical features of resonant tunneling diodes.

2.2.2 Computation of the charge and current density

A first look at the RTD typical potential profile (Fig. 7) brings out the general features of an electron wave function as it traverses the double-barrier structure. The highly doped emitter acts as a reservoir, or Fermi "sea", of electrons for tunneling through the potential barriers. The electron undergoes multiple reflections between the barriers due to its wave nature, leading to a resonance condition of the tunneling when approximately one-half of a de Broglie wavelength equals the well width. The high electric bias field into the collector, which is mainly depleted of negative charges, then sweeps the electrons. Also, there are dimensional changes across the interfaces, i.e., the three-dimensional density-of-states in the emitter and collector versus the two-dimensional density-of-states in the quantum well. Thus, in modeling the resonant tunneling diode, three regions are distinguished.

The emitter and the collector are treated the same way. In both regions it is assumed that a quasi-equilibrium carrier distribution is maintained even when the structure is under voltage bias. It can be justified by the fact that potential barriers tend to isolate these regions from one another and that the coupling with the quantum well is weak, even on resonance, because of the small width of the longitudinal component of the density-of-states in the quantum well. In each region, the quasi-Fermi levels, E_F^e and E_F^c , are defined by the requirement for space-charge neutrality over the entire extent of the device. The Thomas-Fermi local equilibrium treatment of the conduction electrons has proven robust in much of nanostructure modeling [10] and allows the calculation of

the mobile charge in the emitter and the collector:

$$n(x) = N_c \frac{2}{\sqrt{\pi}} F_{1/2} \left[\frac{E_F - E_c(x)}{k_B T} \right]$$

$$\text{with } \begin{cases} F_{1/2}(\eta) = \int_0^\infty \frac{\sqrt{x} dx}{1 + e^{x-\eta}} \\ N_c = 2 \left(\frac{2\pi m^* k_B T}{h^2} \right)^{3/2} \end{cases}$$

However this approach is not suitable for the quantum well region as it assumes electrons are distributed as a 3D free electron gas.

In the quantum well region, electron states are treated purely quantum mechanically. The one-dimensional, time-independent, single-particle, single-band, effective mass Schrödinger equation is used in the direction perpendicular to the quantum-well layers:

$$\left[-\frac{\hbar^2}{2} \nabla_x \left(\frac{1}{m^*(x)} \nabla_x \right) + V(x) \right] \Psi(E, x) = [E - E_c] \Psi(E, x)$$

where E is the longitudinal energy of the particle considered, E_c is the bottom energy of the conduction band, $m^*(z)$ is the effective mass, and $V(z)$ is the potential-energy term including the effects of the device conduction-band offset, the bias voltage applied across the device, and the mobile electronic charge. The crucial assumption made by using the one-dimensional Schrödinger equation is that longitudinal and transverse components of the energy of electrons are decoupled. Both the longitudinal energy of electrons and the length (x -axis) of the device are numerically discretized. Within each spatial increment, the mass and the potential are assumed to be constant so that the Schrödinger equation can be solved with piecewise-continuous plane waves [11]. For electrons incident from left (emitter region) to right (collector region), we have:

$$\begin{cases} \Psi^{l-r}(E, x) = a^{l-r}(E, x) e^{ik_x x} + b^{l-r}(E, x) e^{-ik_x x} & \text{in the quantum well region,} \\ \Psi_e^{l-r} = e^{ik_c x_c} + r^{l-r}(E) e^{-ik_c x_c} & \text{in the emitter right next to the first interface, and} \\ \Psi_c^{l-r} = t^{l-r}(E) e^{ik_c x_c} & \text{in the collector right next to the last interface.} \end{cases}$$

As indicated above, solutions are matched to plane-wave functions in the emitter and the collector with the amplitude of the incident plane-wave function set to unity. This solution does not account for electron flowing from the collector to the emitter. For such electrons:

$$\begin{cases} \Psi^{r-l}(E', x) = a^{r-l}(E', x)e^{-ik_x x} + b^{r-l}(E', x)e^{ik_x x} & \text{in the quantum well region,} \\ \Psi_c^{r-l} = e^{-ik_c x_c} + r^{r-l}(E')e^{ik_c x_c} & \text{in the collector right next to the last interface, and} \\ \Psi_e^{r-l} = t^{r-l}(E')e^{-ik_c x_c} & \text{in the emitter right next to the first interface.} \end{cases}$$

The continuity of the wave function $\Psi^{l-r}(E, x)$ and of its derivative

$[m^*(x)]^{-1} \partial \Psi^{l-r}(E, x) / \partial x$ along the x-axis gives relationships between the amplitude coefficients of the wave function:

$$\begin{aligned} a^{l-r}(E, x_j) &= \frac{1}{2} \left[\left(1 + \frac{Z_{j+1}}{Z_j} \right) a^{l-r}(E, x_{j+1}) \exp(i(k_{x_{j+1}} - k_{x_j})x_j) \right. \\ &\quad \left. + \left(1 - \frac{Z_{j+1}}{Z_j} \right) b^{l-r}(E, x_{j+1}) \exp(-i(k_{x_{j+1}} + k_{x_j})x_j) \right] \\ b^{l-r}(E, x_j) &= \frac{1}{2} \left[\left(1 - \frac{Z_{j+1}}{Z_j} \right) a^{l-r}(E, x_{j+1}) \exp(i(k_{x_{j+1}} + k_{x_j})x_j) \right. \\ &\quad \left. + \left(1 + \frac{Z_{j+1}}{Z_j} \right) b^{l-r}(E, x_{j+1}) \exp(-i(k_{x_{j+1}} - k_{x_j})x_j) \right] \\ \text{with } Z_j &= \frac{k_{x_j}}{m^*(x_j)} \end{aligned}$$

where the subscript j refers to the j^{th} spatial increment. So the Schrödinger equation is solved recursively, from right to left (left to right) for electrons flowing from emitter to collector (collector to emitter), and normalized so that the amplitude of the incident plane wave is unity. The statistical properties of carriers will be addressed in the expressions used to calculate the charge stored in the well and the current density across the structure. A quantity of interest for the current density calculation is the transmission probability of an electron, i.e. its probability to cross through the quantum-well region as a function of its initial longitudinal energy. From time reversal symmetry and the probability-current continuity principles implied by the quantum mechanical treatment, we obtain useful relations among the coefficients r^{l-r} , t^{l-r} , r^{r-l} and t^{r-l} [12]:

$$\begin{aligned}
|r^{l \rightarrow r}(E) &= |r^{r \rightarrow l}(E)| \\
k_c |t^{l \rightarrow r}(E) &= k_e |t^{r \rightarrow l}(E)| \\
\frac{k_c}{k_e} |t^{l \rightarrow r}(E)|^2 + |r^{l \rightarrow r}(E)|^2 &= 1 \\
\frac{k_e}{k_c} |t^{r \rightarrow l}(E)|^2 + |r^{r \rightarrow l}(E)|^2 &= 1
\end{aligned}$$

Thus the transmission probability is the same in both directions given that the energy reference is the same:

$$T(E) = 1 - |r^{l \rightarrow r}(E)|^2 = 1 - |r^{r \rightarrow l}(E)|^2$$

An important remark about the discretization of the Schrödinger equation has to be made. Although the spatial increments are made uniform for technical reasons explained later, the energy discretization is made “adaptive”. The transmission function as well as the wave function feature sharp peaks around the values of the energy levels in the quantum well(s). The energy increments are made finer around those energies to achieve a good resolution of the transmission peak. This is done by linking the energy increments to the slope of the transmission function. This adaptive stepping technique saves a tremendous amount of computation time and refines the calculation around the energies that contribute most to the current density and the electronic charge density.

The current density can be evaluated using the Tsu-Esaki formula [13], which can be explained as follow [14]. Planes waves incident from the emitter having longitudinal energy E and transverse energy E_t carry a statistical weight $f_e(E + E_t)$, where f_e is the Fermi-Dirac distribution in the emitter. They give rise to an incident electron current contribution from a unit volume of k-space:

$$j_i = \frac{2e}{(2\pi)^3} f_e(E + E_t) \frac{1}{\hbar} \left(\frac{\partial E}{\partial k_e} \right)_E$$

with the factor 2 in the numerator accounting for spin and the $(2\pi)^2$ for the density of states in k-space. The last term represents the group velocity of the plane wave. To contribute to the transmitted flux this plane wave must not only couple to a state on the other side of the structure, but because electrons are fermions, that state must be empty. The transmitted electron current contribution is then:

$$j_t = \frac{2e}{(2\pi)^3} f_e(E + E_t) [1 - f_c(E + \Delta V + E_t)] T(E) \frac{1}{\hbar} \left(\frac{\partial E}{\partial k_e} \right)_E$$

where $f_c(E + \Delta V + E_t)$ is the Fermi-Dirac distribution in the collector and ΔV the potential energy drop between the emitter and the collector or the longitudinal kinetic energy gained by an electron after crossing the quantum-well region. If all energy levels are referenced to the same point, we have:

$$\begin{cases} E_F^e - E_F^c = V_{bias} \\ f_e(E + E_t) = \left[1 + \exp\left(\frac{E + E_t - E_F^e}{k_B T}\right) \right]^{-1} \\ f_c(E + \Delta V + E_t) = \left[1 + \exp\left(\frac{E + E_t - E_F^c}{k_B T}\right) \right]^{-1} \end{cases}$$

V_{bias} is the fraction of applied voltage that drops across the structure. The total electron current density flowing from left to right is obtained by integrating over the longitudinal and transverse wave vector, k_e and \bar{k}_t , of electrons in the emitter.

$$J^{l-r} = \iiint \frac{2e}{(2\pi)^3} f_e(E + E_t) [1 - f_c(E + \Delta V + E_t)] T(E) \frac{1}{\hbar} \left(\frac{\partial E}{\partial k_e} \right)_E dk_e d\bar{k}_t$$

To be able to partially integrate this equation analytically, we assume that the transverse dispersion relationship is parabolic:

$$E_t = \frac{\hbar^2 k_t^2}{2m_e^*}$$

After a change of variable, the expression used in the simulation is obtained:

$$J^{l-r} = \frac{em_e^* k_B T}{2\pi^2 \hbar^3} \int T(E) \ln \left(\frac{1 + e^{\frac{E_F^c - E}{k_B T}}}{1 + e^{\frac{E_F^e - E}{k_B T}}} \right) \frac{\left(\frac{\partial E}{\partial k^e} \right)_E dk^e}{1 - e^{\frac{E_F^c - E_F^e}{k_B T}}}$$

The same kind of analysis allow one to obtain the current density for electrons flowing from right to left:

$$J^{r-l} = \frac{em_e^* k_B T}{2\pi^2 \hbar^3} \int T(E) \ln \left(\frac{1 + e^{\frac{E_F^c - E}{k_B T}}}{1 + e^{\frac{E_F^e - E}{k_B T}}} \right) \frac{\left(\frac{\partial E}{\partial k^e} \right)_E dk^e}{1 - e^{\frac{E_F^c - E_F^e}{k_B T}}}$$

The total electron current density is given by:

$$J^{total} = J^{l-r} - J^{r-l}$$

It can be checked that this current density goes to zero when no bias voltage is applied,

and that the component J^{r-l} becomes negligible as an increasing positive bias voltage is applied.

The electron density in the quantum well region is also calculated by considering two streams of electrons impinging from the emitter and the collector, respectively [15]. For the left-to-right electron flow, the modulus square of the wave function is used to determine how electrons in the Quasi-Fermi sea on the emitter side spread into the quantum well region:

$$\begin{aligned} n^{l-r}(x) &= \iiint \frac{2}{(2\pi)^3} |\Psi^{l-r}|^2(E, x) f_e(E + E_t) dk_e d\vec{k}_t \\ &= \frac{m_e^* k_B T}{2\pi^2 \hbar^2} \int |\Psi^{l-r}|^2(E, x) \ln \left(1 + e^{\frac{E_F^e - E}{k_B T}} \right) dk_e \end{aligned}$$

Again the transverse component of the wave vector has been integrated analytically. A similar expression is derived for the stream of electrons flowing from right to left:

$$\begin{aligned} n^{r-l}(x) &= \frac{m_e^* k_B T}{2\pi^2 \hbar^2} \int |\Psi^{r-l}|^2(E, x) \ln \left(1 + e^{\frac{E_F^c - E}{k_B T}} \right) dk_c \\ \text{and } n^{total}(x) &= n^{l-r}(x) + n^{r-l}(x) \end{aligned}$$

It is important to remark about the boundaries of integration in the expressions of the current density and the electron density. When the RTD is biased positively, more and more charge accumulates just before the first heterointerface in the low-doped part of the emitter. The potential profile in this section of the structure presents a triangular-like quantum well feature, and quantized levels should be formed. The inclusion of this additional quantization is tedious and not compatible with the Tsu-Esaki formula (which assumes a 3D Fermi distribution in the emitter) [16]-[17]. Therefore for the sake of simplicity, only states above the top of the conduction-band-edge maximum are accounted for in the current and electron density calculations (as illustrated in Fig. 7). This simplification is not as bad as it first appears. Electrons with a small longitudinal energy have only a small contribution to the current density, as their group velocity is also small. We believe this approximation does not affect much the overall current density, though it has an impact on the voltage range of the negative differential resistance region.

We now have physical models for the current density and the electron density along the entire structure. Both have to be coupled to the Poisson equation to determine the physical characteristics of the resonant tunneling diodes.

2.2.3 Computational method

The model presented above was used to determine the electronic charge density from the potential profile. With the Poisson equation these equations form a self-consistent set of equations:

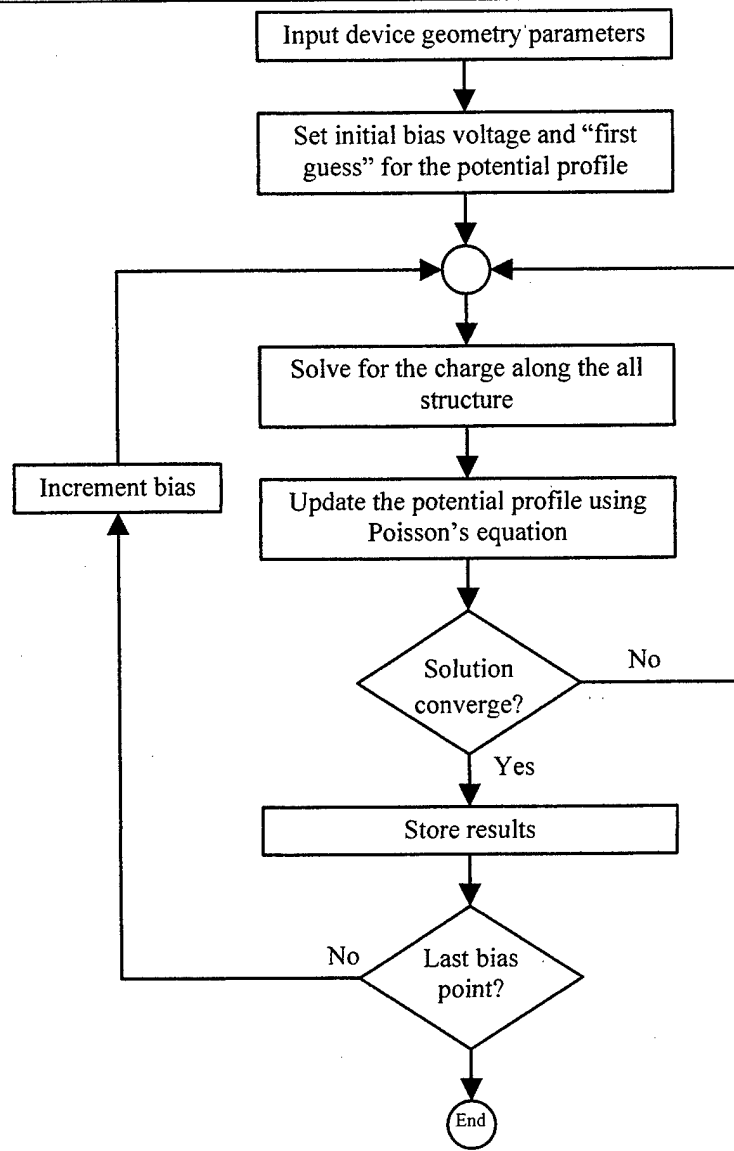


Fig. 8 Flowchart of the computational method

$$\begin{cases} n(x) = f(V(x)) & \text{where } f \text{ is determined either by } \begin{cases} \text{Thomas-Fermi distribution} \\ \text{Schrodinger equation} \end{cases} \\ \frac{d^2V}{dx^2}(x) = -\frac{en(x)}{\epsilon_s(x)} & \text{with } \begin{cases} V(0) = 0 \\ V(L) = -V_{bias} + \Delta E_F \end{cases} \end{cases}$$

where ΔE_F is a constant related to the difference of doping between the ends of the collector and emitter.

The first step is to discretize the Poisson equation to transform the differential equation into a linear equation [18]:

$$\begin{cases} \frac{\partial^2 V}{\partial x^2}(x) = -\frac{en(x)}{\epsilon_s(x)} \\ V(0) = 0 \\ V(L) = -V_{bias} + \Delta E_F \end{cases} \longrightarrow \begin{cases} \frac{V_{j+1} - 2V_j + V_{j-1}}{\Delta x^2} = f_j & 0 \leq j \leq N-1 \\ V_{-1} = 0 \\ V_N = \bar{V} \equiv -V_{bias} + \Delta E_F \end{cases}$$

Because of the uniform spatial increments, the Poisson equation can then be expressed in a matrix form:

$$A\bar{V} = \Delta x^2 \bar{f} - \bar{b}$$

$$\text{with } \begin{cases} A = \begin{pmatrix} -2 & 1 & & & \\ 1 & \ddots & \ddots & & \\ & \ddots & \ddots & 1 & \\ & & 1 & -2 & \end{pmatrix} \\ \bar{V} = \begin{pmatrix} V_0 \\ \vdots \\ V_{N-1} \end{pmatrix}, \bar{f} = \begin{pmatrix} f_0 \\ \vdots \\ f_{N-1} \end{pmatrix}, \bar{b} = \begin{pmatrix} 0 \\ \vdots \\ \bar{V} \end{pmatrix} \end{cases}$$

The matrix A can be easily inverted and we have a direct linear relationship to calculate the potential profile from the charge profile along the structure at a given voltage bias.

We now have a system of two algebraic equations, which explicitly relate the charge density and potential profile to one another, to resolve. The simplest convergence algorithm one can think of is presented in Fig. 8 [19]-[20]. For a given bias voltage, a first guess of the potential profile is made. The charge density along the structure is calculated. Then a new potential profile is calculated thanks to the Poisson equation. If all the points of this new potential profile are within a pre-determined margin of the old potential profile, the system has converged. If it is not the case, this new potential is launched back into the loop until convergence is achieved. Once a solution is obtained for a given voltage bias, this solution makes a good first guess for the following bias point.

Actually this algorithm does not give satisfying results. It is too unstable and solutions tend to diverge. Even the addition of a relaxation factor is not sufficient to stabilize the system. That is the reason why the addition of an acceleration method [21]-[22] has proven to be necessary. The whole process of solving the Poisson and charge density equations may be regarded as an operator H transforming V^k into W^k :

$$W^k = HV^k$$

where V^k is the k^{th} iteration of the unknown potential profile and W^k is the potential profile calculated from V^k . The basic algorithm, where no acceleration method is present, can be expressed as follow:

$$V^{k+1} = W^k$$

The idea underlying the acceleration method is to use W^k , along with the V 's and W 's

stored during the previous iteration, to evaluate the new, optimized, iteration as:

$$V^{k+1} = F(V^k, W^k, V^{k-1}, W^{k-1}, \dots)$$

The purpose of the function F is to build up an iterative sequence that converges more rapidly than the basic sequence. The acceleration method works as follows. Define

$$a^k = V^k + \sum_{j=1}^M \alpha_j^k (V^{k-j} - V^k)$$

$$b^k = W^k + \sum_{j=1}^M \alpha_j^k (W^{k-j} - W^k)$$

where M is the number of previously stored iterates, and α_j^k 's are free parameters. The latter are chosen in order to minimize the residual

$$R^k(\alpha_1^k, \dots, \alpha_M^k) = \frac{1}{2} \sum_{i=1}^N (a_i^k - b_i^k)^2$$

where N is the dimension of V^k . In turn, minimizing R^k requires the algebraic system of order M

$$\frac{\partial R^k}{\partial \alpha_j^k} = 0 \quad j = 1, \dots, M$$

to be solved. Finally the new iterate V^{k+1} is defined as

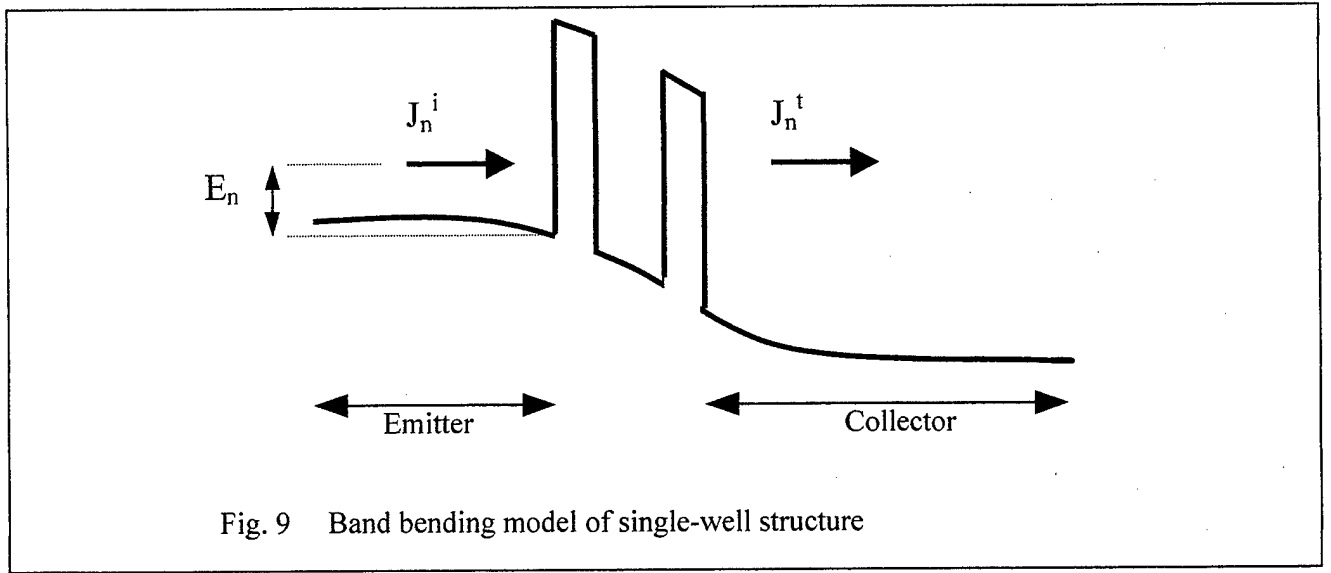
$$V^{k+1} = a^k + \beta(b^k - a^k) \quad 0 < \beta \leq 1$$

where β is the relaxation parameter. The simulations have been carried out with $M = 5$ and β has been varied according to the fastest convergence time for each structure under investigation.

The convergence criterion used is that the calculated potential must be within 0.5 meV of the previous calculated potential. Self-consistent solutions are obtained in a few tens of second on a 2 GHz machine after 5 to 20 iterations, depending on the length of the structure and the bias voltage at which the calculation is made. The modeling of the current-voltage characteristics of resonant tunneling diodes is only the first step of the simulation procedure for determining the noise characteristics, presented in the next section.

2.3 Noise mechanisms in RTDs

Two noise mechanisms must be considered in resonant tunneling diodes: thermal noise and shot noise.



2.3.1 Thermal noise

Thermal noise is caused by the scattering of carriers with a lattice and is directly proportional to the temperature of the thermodynamic bath in which they reside. Once the I-V characteristic of the RTD is known, the spectral density of current fluctuations for thermal noise can be immediately estimated from Nyquit's generalized formula:

$$S_I = 4k_B T G$$

where k_B is Boltzman's constant, T is the device temperature, $G = \text{Re}\{Y\}$ and Y is the differential admittance. Thus it appears that the thermal noise power increases with the absolute value of the slope of the I-V curve.

2.3.2 Shot noise

Shot noise is a type of fluctuation in the electrical current that is observed in many electronic devices operating out of thermodynamic equilibrium. In most cases it is associated with randomness in the flux of carriers crossing a barrier in the device. The source of this randomness is thermal fluctuations in the rate of carrier injection into the barrier. At frequencies small compared to the reciprocal of the transit time across the active layer, the power spectral density of such shot noise is given by $S_I = 2e\gamma I$, where I is the average current, e is the magnitude of the electronic charge, and γ is the shot noise factor.

In the majority of devices it is found that $\gamma = 1.0$, which is the condition of normal, or full, shot noise. Some examples are p-n diodes, Schottky diodes, and single hetero-barrier diodes. In these devices the potential energy barrier has transmission characteristics that are independent of the current magnitude. The carrier-injection times into the active layer obey a Poissonian distribution. This implies that these injection times are statistically independent and that the transit of a carrier across the active layer is an event fully uncorrelated to the transit of other carriers. Therefore, the arrival times of carriers on the collector side of the active layer obey Poisson statistics, leading to the full shot noise in the terminal current fluctuations.

In devices having a potential barrier whose transmission depends on the current, significant deviation from full shot noise can occur. The classic example is the space-

charge-limited vacuum diode in which the barrier consists of a spatial distribution of electrons located near the cathode [23]. In double-barrier resonant tunneling diodes, shot noise reduction ($\gamma < 1.0$) [24]-[27] and shot noise enhancement ($\gamma > 1.0$) [27] have been observed. The primary assumption of the following derivation is that the physical basis of the shot noise reduction and enhancement is the modulation of the double-barrier transmission probability by the charge stored in the quantum well. Notably the charge in the well induces correlations between the fluctuations of the incident current in different energy intervals. This effect will be more clearly explained in the presentation of the analytical model of shot noise used in this work.

2.4. Modeling of shot noise in RTDs

2.4.1. Analytic Modeling

Let us consider a single-well resonant tunneling diode biased with a large enough voltage so that a wide depleted space-charge region forms on the collector side and excess electrons accumulate on the emitter side. Under this bias condition, the current through the diode consists of electrons that are incident on the double-barrier structure from the emitter side and are transmitted through the structure by resonant tunneling through the first or higher quasi-bound levels of the quantum well. J_i denotes the total time-averaged electronic flux incident on the double-barrier structure from the emitter side, and J_t denotes the transmitted flux. These fluxes can be decomposed into components J_n^i and J_n^t contained within specified intervals of energy ΔE_n along the tunneling direction (Fig. 9). The energy is referenced to the conduction band edge on the emitter side. The magnitude of the time-averaged electrical current through the diode is related to the incident flux by:

$$I = \sum_n eJ_n^t = \sum_{n,m} eT_{nm}J_m^i \equiv \sum_m eT_mJ_m^i = \sum_m I_m^e$$

where T_{nm} is the transmission probability through the double-barrier structure of an electron incident in the m th energy interval and transmitted to the n th interval, and I_m^e is the electrical current flowing in the m th interval on the emitter side. We assume the resonant tunneling is elastic, so that

$$T_{nm} = 0 \text{ for } m \neq n \quad \text{and} \quad J_n^t = T_n J_n^i$$

However the formalism developed is valid independent of the coherent or sequential nature of the resonant tunneling. For the purpose of analyzing the shot noise, fluctuations in the current and the fluxes are defined in the usual sense as the difference between the instantaneous and the average value of each quantity. All fluctuations are assumed to occur under the condition of an ac short circuit across the diode.

The source of the shot noise is the fluctuation of the incident flux in each energy interval. A given component ΔJ_n^i has two effects on the transmitted current. First, it contributes directly to the transmitted current through the term $T_n \Delta J_n^i$. Second it modulates the transmission probability in other energy intervals by varying the charge density, and hence the potential profile, in the double-barrier structure. To first order, the

fluctuation in the diode current due to fluctuations in all intervals is

$$\Delta I = \sum_n e T_n \Delta J_n^i + \sum_{n,m} e J_n^i \frac{\partial T_n}{\partial J_m^i} \Delta J_m^i$$

Since the fluctuation ΔJ_n^i occurs independently of T_n , one can define $\Delta I_n^e = e T_n \Delta J_n^i$. It follows that

$$\Delta I = \sum_n \Delta I_n^e + \sum_{n,m} C_{nm} \Delta I_m^e$$

where $C_{nm} = J_n^i (\partial T_n / \partial J_m^i) T_m^{-1}$. The quantity C_{nm} is an element of a matrix that represents the modulation of the transmission at each energy by fluctuations of the incident current at other energies.

The low-frequency spectral density of the total current fluctuation is found to be

$$S_I = \frac{\overline{(\Delta I)^2}}{\delta f} = \frac{1}{\delta f} \left[\overline{\left(\sum_n \Delta I_n^e \right)^2} + \sum_k \Delta I_k^e \sum_{n,m} C_{nm} \Delta I_m^e + \overline{\left(\sum_{n,m} C_{nm} \Delta I_m^e \right)^2} \right]$$

This expression is simplified with the following assumptions. First, incident current fluctuations in different longitudinal energy intervals are uncorrelated [23]

$$\overline{\Delta I_n^e \Delta I_m^e} = \delta_{nm} \overline{[\Delta I_n^e]^2}$$

where δ_{nm} is the Kronecker delta function. Second, the incident current component fluctuations are Poisson-distributed and are thus related to the average component by the well-known Schottky relation [1]:

$$\overline{[\Delta I_n^e]^2} = 2e I_n^e \delta f$$

The application of these relations leads to the result

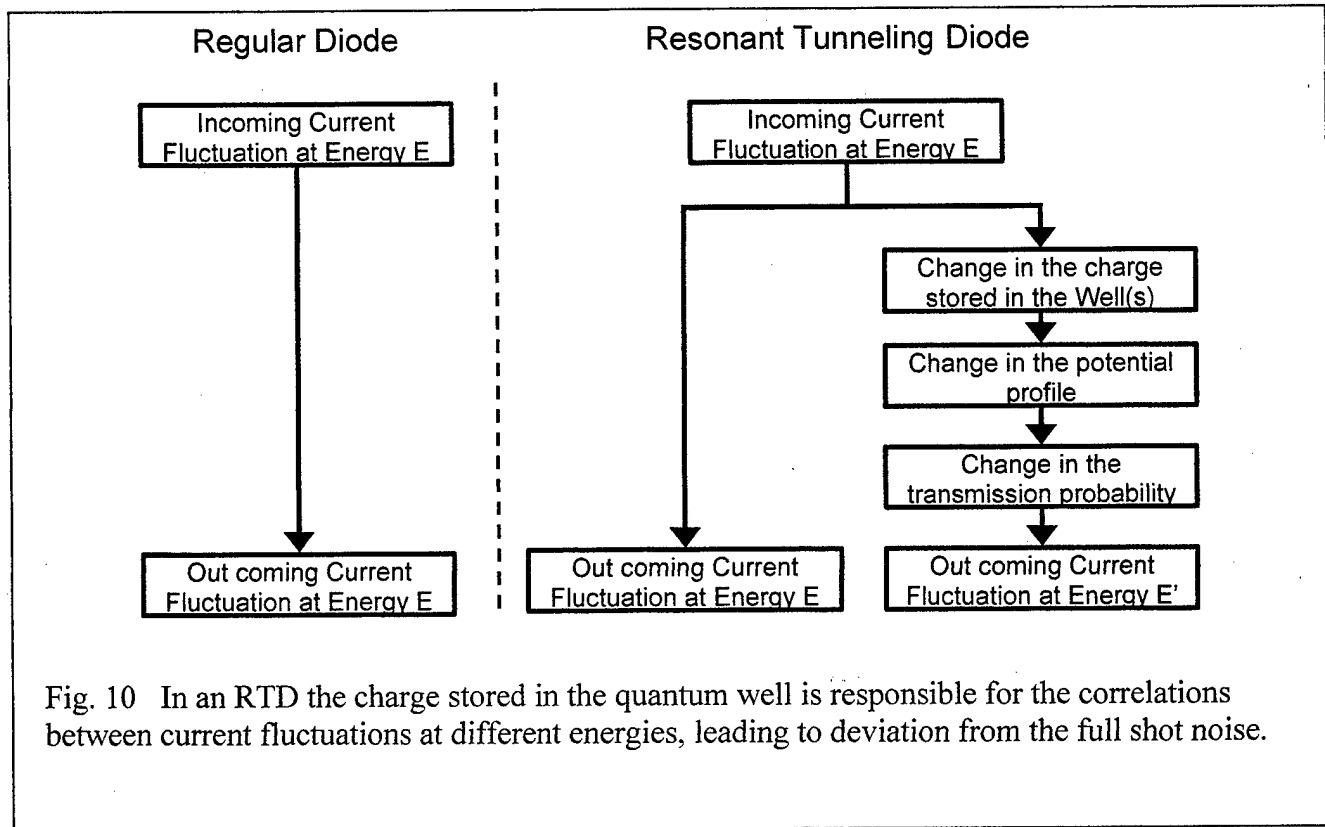
$$S_I = 2eI \left[1 + 2I^{-1} \sum_{n,m} C_{nm} I_m^e + \sum_m \left(\sum_n C_{nm} \right)^2 I_m^e \right] \equiv 2eI\gamma$$

In the limit that $\Delta E_n \rightarrow 0$ for all n , γ can be written in integral form as

$$\gamma = 1 + 2I^{-1} \int_{E'} \left[\int_E dC(E, E') \right] dI^e(E') + I^{-1} \int_{E'} \left[\int_E dC(E, E') \right]^2 dI^e(E')$$

where $dC(E, E') = dJ^i(E) \left[\partial T(E) / \partial J^i(E') \right] T^{-1}(E')$

and $I = \int_E dI^e(E) = \int_E eT(E) dJ^i(E)$



This equation is the basis of the following simulations to investigate shot noise in multiple-well resonant tunneling diodes.

2.4.2. Numerical Modeling

The numerical calculation of the shot noise factor requires the calculation of each element of the correlation matrix $dC(E, E')$. The only part that is not readily available is the derivative $\partial T(E)/\partial J'(E')$. This term represents the impact of an incident current fluctuation at energy E' on the transmission probability at energy E , which is related to the amount of charge injected into the well(s) due to this current fluctuations (Fig. 10). It is calculated using the following procedure using the chain rule of differential calculus:

$$\frac{\partial T(E)}{\partial J'(E')} \approx \frac{\Delta T(E)}{\Delta J'(E')} = \frac{\Delta T(E)}{\Delta n(x)} \frac{\Delta n(x)}{\Delta J'(E')}$$

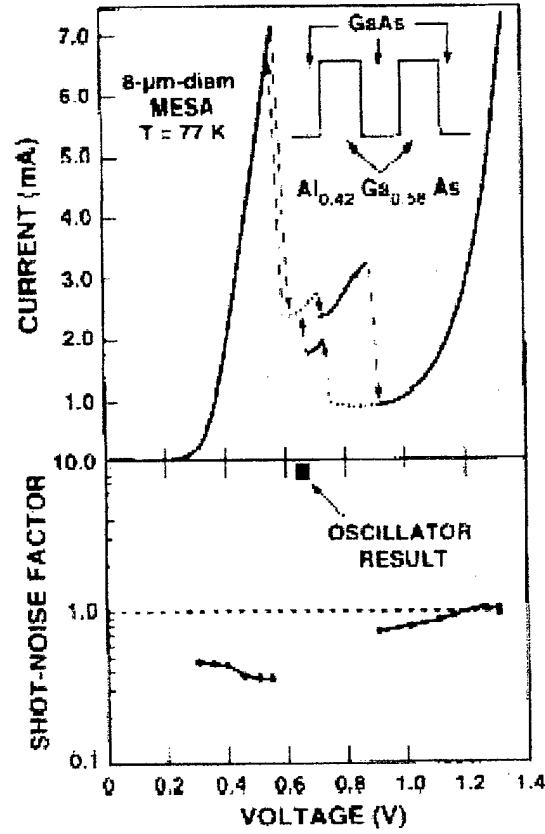


Fig. 11 Experimental I-V curve and shot noise factor measurements of a single-well resonant tunneling diode made from GaAs/AlGaAs

First a current fluctuation $\Delta J'(E')$ is properly picked so that the resulting shot noise factor is independent of this choice. This is accomplished by choosing $\Delta J'(E')$ so that the amount of charge injected due to this current fluctuation is kept a constant fraction of the average amount charge in the well at the bias voltage at which the computation is made. This fluctuation gives rise to a fluctuation $\Delta n(x)$ of the charge in the quantum well. By identification with the current density formula, we have:

$$n(x) = \int \frac{\hbar |\Psi^{l-r}|^2(E, x) \left(1 - e^{-\frac{E_F^e - E_F^r}{k_B T}} \right) \ln \left(1 + e^{\frac{E_F^e - E}{k_B T}} \right)}{\ln \left(\frac{1 + e^{\frac{E_F^e - E}{k_B T}}}{1 + e^{\frac{E_F^e - E}{k_B T}}} \right) \left(\frac{\partial E}{\partial k^e} \right)_E} dJ'(E)$$

100 nm In _{0.53} Ga _{0.47} As N _D =1.3 x 10 ¹⁹ cm ⁻³
100 nm In _{0.53} Ga _{0.47} As N _D =2.0 x 10 ¹⁸ cm ⁻³
5 nm In _{0.53} Ga _{0.47} As N _D =2.0 x 10 ¹⁶ cm ⁻³
1.1 nm AlAs UNDOPED
5.6 nm In _{0.53} Ga _{0.47} As UNDOPED
1.4 nm AlAs UNDOPED
75 nm In _{0.53} Ga _{0.47} As N _D =1.0 x 10 ¹⁷ cm ⁻³
200 nm In _{0.53} Ga _{0.47} As N _D =2.0 x 10 ¹⁸ cm ⁻³
200 nm In _{0.53} Ga _{0.47} As N _D =1.3 x 10 ¹⁹ cm ⁻³
N ⁺ InP SUBSTRATE

Fig. 12 Epitaxial-layer profile of the test structure made from In_{0.53}Ga_{0.47}As/AlAs. Note that the thicknesses of the top barrier and quantum well are slightly less than the nominal (MBE growth) values, consistent with the theoretical results given here.

$$\text{thus } \frac{\partial n(x)}{\partial J^i(E')} = \frac{\hbar |\Psi^{l-r}|^2(E', x) \left(1 - e^{\frac{E_F^c - E_F^e}{k_B T}} \right) \ln \left(1 + e^{\frac{E_F^c - E'}{k_B T}} \right)}{\ln \left(\frac{1 + e^{\frac{E_F^c - E'}{k_B T}}}{1 + e^{\frac{E_F^c - E'}{k_B T}}} \right) \left(\frac{\partial E}{\partial k^e} \right)_{E'}}$$

$$\text{and } \Delta n(x) = \frac{\partial n(x)}{\partial J^i(E')} \Delta J^i(E')$$

Here we assumed that only current flowing from emitter to collector gives rise to shot noise, which should be a good approximation as long as the bias voltage is not too close to zero.

The charge fluctuation $\Delta n(x)$ modifies the potential profile of the device. If we assume the depletion region in the collector is not affected by this charge fluctuation (because positive charges are not affected by the fluctuation), the Poisson equation can be integrated using as boundary conditions the value of the electric field at the collector / quantum well region interface and the value of the potential at the emitter end as boundary conditions. A new transmission function is then obtained from this modified potential profile, allowing the calculation of $\Delta T(E)$. This numerical procedure can be very intensive in computer resources because: (1) the correlation matrix is not symmetric and each matrix element must be calculated individually, and (2) the number of matrix elements is equal to the square of the number of energy intervals and the number of energy intervals must be a three-to-four digit number to obtain a reasonable precision.

2.4.3. Physical Interpretation

A typical shot noise characteristic of a single-well RTD is presented in Fig. 11. These data [2] were measured for a GaAs/AlGaAs structure at 77 K and are

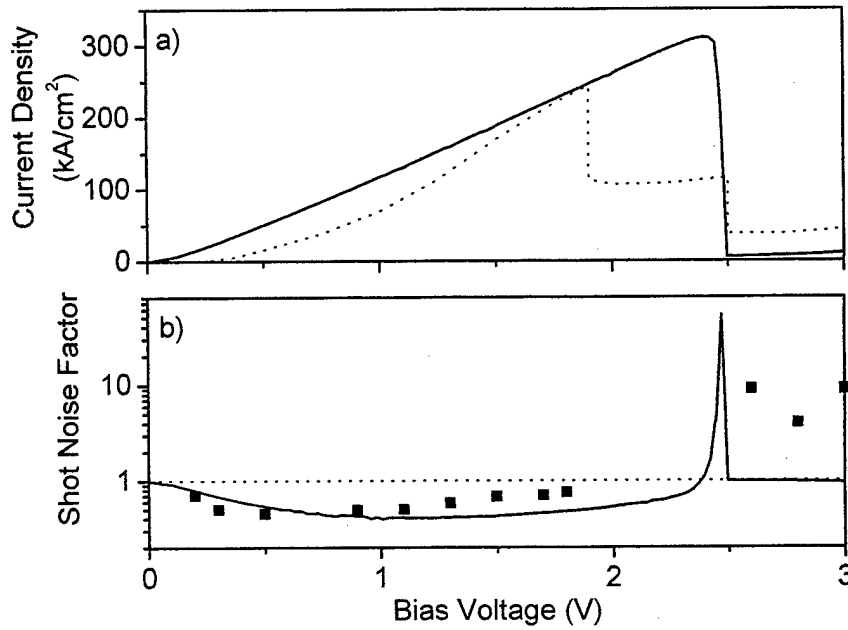


Fig. 13 Results for InGaAs/As test structure: (a) current density, and (b) shot noise factor vs. bias voltage. Dotted line and squares are the experimental results; solid curves are the simulation results.

representative of the behavior of single-well RTDs. In the positive differential resistance region, shot noise reduction ($\gamma < 1$) is observed. In the negative differential resistance region, shot noise enhancement ($\gamma > 1$) is observed. Based on the formalism developed it can be explained as follows. A positive fluctuation of the incident current injects more mobile electronic charge in the quantum well. Through the Poisson equation, this injected charge modifies the potential profile of the structure, causing the quasi-bound levels of the quantum well to shift. This then impacts the transmission probability of electrons in the emitter in a manner depending on the bias region of the device.

In the positive differential resistance region (PDR), a positive current fluctuation shifts up the quasi-bound level of the quantum well to an energy at which there are fewer electrons to tunnel from the emitter side. This is because in the PDR region the quasi-bound level is aligned with the Fermi sea on the emitter side so an increase in energy corresponds to a reduction in the Fermi-Dirac probability. Thus the instantaneous total current is decreased by the fluctuation, leading to shot noise reduction.

In the negative differential resistance region (NDR), it shifts up the quasi-bound level to an energy at which there are more electrons to tunnel. This is because in the NDR region the quasi-bound level is aligned below the conduction-band edge of the Fermi sea on the emitter side so an increase in energy corresponds to an increase in Fermi-Dirac probability. An increase of the instantaneous total current is then caused by the fluctuation, leading shot noise enhancement.

It is also appropriate to ask what the meaning is of shot noise reduction and enhancement in a more general sense. When there is full shot noise ($\gamma = 1$), the emission and collection times of carriers through the structure follow a Poissonian distribution. Thus they are both fully independent statistical variables. It means the collection of carriers is a fully random process and each collection event is independent from the

200 nm InGaAs, $N_D=5 \times 10^{18}$
200 nm InGaAs, $N_D=2 \times 10^{18}$
200 nm InGaAs, $N_D=2 \times 10^{16}$
BARRIERS AND WELL(s)
200 nm InGaAs, $N_D=2 \times 10^{16}$
200 nm InGaAs, $N_D=2 \times 10^{18}$
200 nm InGaAs, $N_D=5 \times 10^{18}$
N^+ InP Substrate

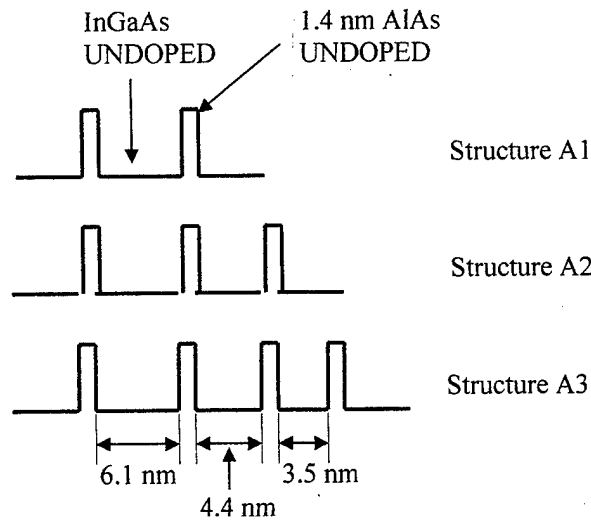


Fig. 14 Design of the three InGaAs/AlAs RTDs under investigation

others. The introduction of the quantum well causes correlations between the collection times of carriers. In the case of shot noise reduction, these correlations are negative and tend to reduce the randomness of the collection of carriers. In the limit that the shot noise is totally suppressed, the carriers would be collected at a perfectly constant rate, a carrier being collected exactly every τ seconds where $\tau = e/I$ and I is the average current through the structure. Shot noise enhancement is more difficult to interpret. Since normal shot noise is already a fully random process, shot noise enhancement cannot be regarded as a more random process. Let us just say that the correlations between the collection times of carriers become positive, and thus the fluctuations of the device terminal current are amplified. This results in an increase of the noise spectral density from the device.

2.4.4. Comparision of numerical model and experiment

The previous sections developed an elaborate model to study the noise properties of resonant tunneling diodes. The validity of the model must be confirmed by comparison of simulation to experiments. The present analysis is limited to coherent tunneling at room temperature because of the relative simplicity of the coherent case and because coherent tunneling generally defines the best possible electrical performance of RTDs. The test structure used to validate the model was originally used to fabricate an oscillator [4] and the data on shot noise are unpublished. The test structure is an $\text{In}_{0.53}\text{Ga}_{0.47}\text{As}/\text{AlAs}$ double-barrier RTD at $T = 300$ K. The structure was grown by molecular-beam epitaxy and fabricated into 4- μm -diam mesa-isolated diodes. The material structure is shown in Fig. 12. The barriers were made very thin and the doping concentration on the emitter (top) side very large to obtain high current density, as evidenced by the peak value of approximately $2.5 \times 10^5 \text{ A-cm}^{-2}$ in the experimental I-V curve of Fig. 13(a). For the present purposes, the noise power from the packaged diodes was measured around 1 GHz. The thermal noise was subtracted from the total noise power to obtain the shot noise factor at selected bias points as plotted in Fig. 13(b). As in previous measurements, the shot noise is suppressed ($\gamma < 1$) at bias voltages below the NDR region and is enhanced above the NDR region. In the present measurements no results were obtained within the NDR region because of the difficulty in suppressing

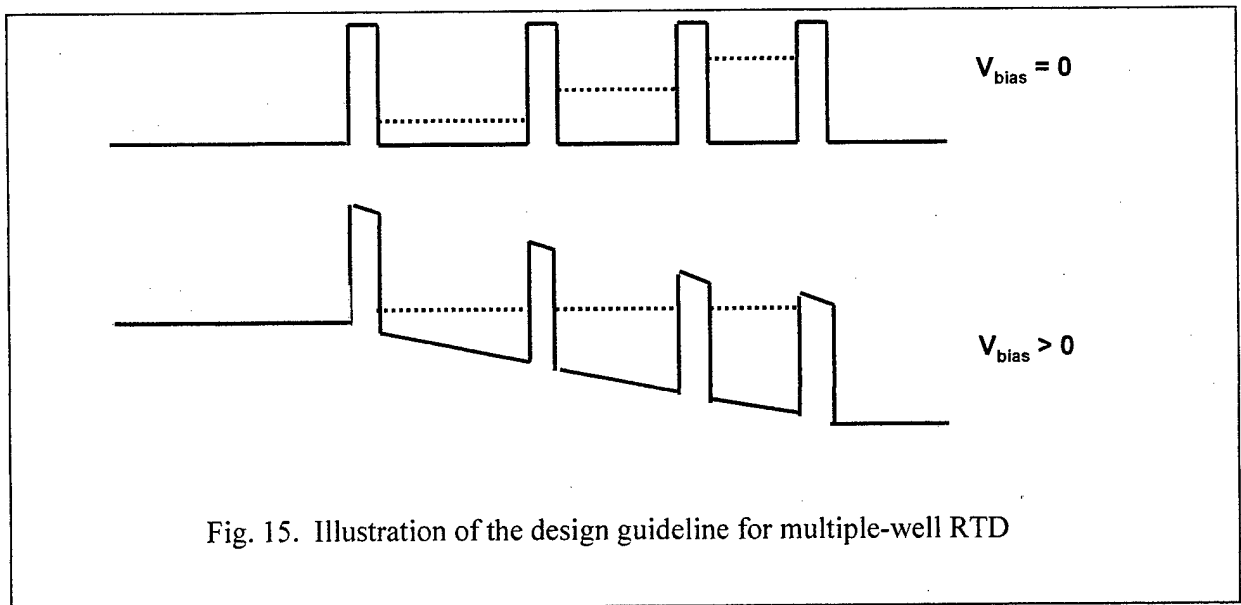


Fig. 15. Illustration of the design guideline for multiple-well RTD

oscillations.

The predictions of the present simulations are plotted against experiment in Fig. 13. The agreement is good for both the I-V characteristic and shot noise factor. The voltage at which the NDR region occurs is well predicted given the facts that: (1) the plateau observed experimentally between 1.9 V and 2.5 V is probably caused by self-rectification of oscillations with the external circuit which distort the NDR region, and (2) as pointed out in reference [16] an overestimation of the current peak and an abrupt NDR region is to be expected when the assumption of the decoupling of the longitudinal and transverse energies is made. Moreover the simulation exhibits some bistability effect in the NDR region, not shown in Fig. 13 but addressed in Appendix 2, consistent with the experimental results. The shot noise factor is also qualitatively and quantitatively well predicted. Notably the minimum measured shot noise factor is $\gamma^{\min} = 0.45$ and the minimum simulated value is $\gamma^{\min} = 0.39$.

The bulk of the disparities between simulation and experiment can be attributed to different causes. First the physical model treats the emitter and the collector semi-classically, and the quantum well region fully quantum mechanically. A quantum mechanical treatment of the entire structure would be more accurate but requires the introduction of heuristic scattering potentials to obtain charge conservation, and raises issues of boundary conditions of open systems that are still not fully understood today. The main shortcoming of the present treatment is that the quantum-size effects related to the formation of the accumulation layer at the emitter / double-barrier interface are neglected. We believe it is a small effect, although it is likely to change the position of the NDR region. Scattering is also neglected but that seems to be a reasonable assumption for the structures under investigation that have very thin potential barriers. Finally the single-band model does not account for tunneling through the X-valley. But that, too, may be negligible because of the thin barriers [28]-[29].

Despite its many simplifications, our model displays reasonable agreement with experiments, and thus allows us to study shot noise in more complicated (multiple-well) structures.

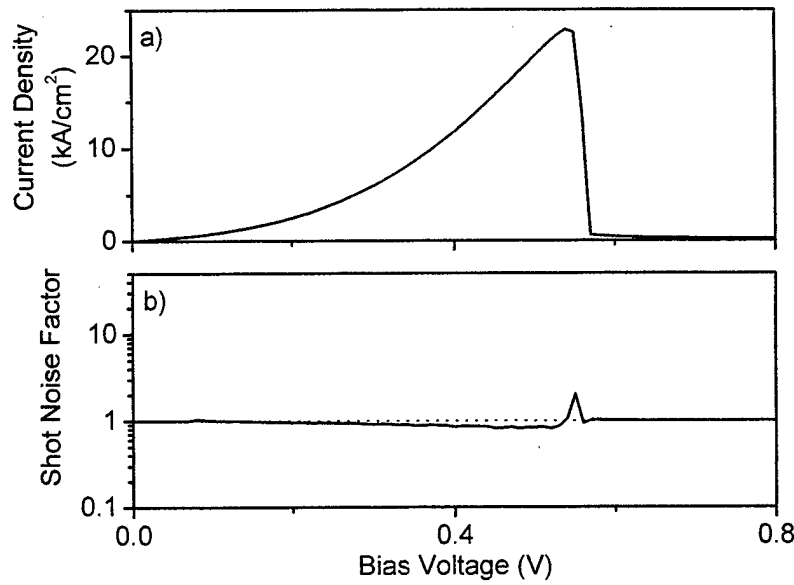


Fig. 16 Structure A1: single-well RTD – (a) computed current density, and (b) shot noise factor vs. bias voltage. The shot noise factor reaches a minimum of 0.81 and a maximum of 2.0

2.5. Simulation of shot noise in multiple-well RTDs

2.5.1. InGaAs/AlAs Structures

The shot noise factor and I-V characteristics are computed at room temperature for three different $\text{In}_{0.53}\text{Ga}_{0.47}\text{As}/\text{AlAs}$ structures all sharing the same emitter and collector layers (Fig. 14) and having potential barriers 1.4 nm wide. Structure A1 is a double-barrier single-well RTD with a 6.1 nm wide well, structure A2 is a triple-barrier RTD with 6.1 nm and 4.5 nm wells, and structure A3 is a quadruple-barrier RTD with 6.1 nm, 4.5 nm and 3.6 nm wells. Structures A2 and A3 are designed with graded well widths (the narrowest well on the collector end) so that the ground-state energies of the three wells gradually come into co-alignment as the bias voltage is increased. With this so-called graded quantum-well technique [30]-[31] (Fig. 15), the peak current density can be made usefully high if the co-alignment occurs while the states are dropping through the Fermi sea on the emitter side. The wells and barriers of all three structures are assumed to be very thin to maximize the likelihood of coherent transport without scattering and, thereby, justify a key assumption of our model.

The predictions of our model for structures A1, A2, and A3 are plotted in Figs. 16, 17, and 18, respectively. Each structure exhibits about the same peak current density of around $2 \times 10^4 \text{ A-cm}^{-2}$. The shot noise factor curves are qualitatively similar, but the shot noise reduction effect is greatly enhanced in the multiple-well structures. The minimum shot noise factor computed in the PDR region of (the single-well) structure A1 is 0.81. This γ^{\min} drops to 0.44 and 0.24 in structures A2 and A3, respectively. We attribute this decrease to the fact that, in structures having the same peak current density, the total amount of charge in the quantum well region increases with the number of wells. This increases the electrostatic repulsion encountered by the injected carriers and thus

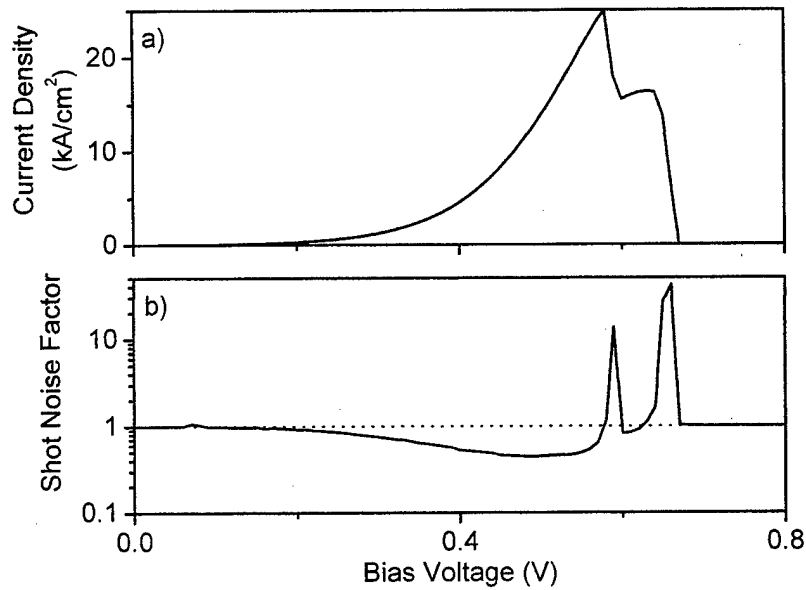


Fig. 17 Structure A2: double-well RTD (a) current density and (b) shot noise factor vs. bias voltage. The shot noise factor is close to its minimum of 0.44 over a rather large voltage range from 0.45 V to 0.55 V. The two peaks in the shot noise factor curve at 0.59 V and 0.66 V mark the crossing of the two transmission function peaks below the Fermi sea.

increases the negative correlations responsible for the shot noise reduction effect.

Fig. 19 shows the minimum shot noise factor versus number of wells in the structure. There is clearly a decreasing trend that leads us to ask whether this result could significantly impact the overall noise performance of a real device made from such structures. Because most devices do not operate under thermodynamic equilibrium, there is no fundamental limit (equivalent to Shannon theorem) for the shot noise reduction effect. But this argument neglects the contribution from thermal noise.

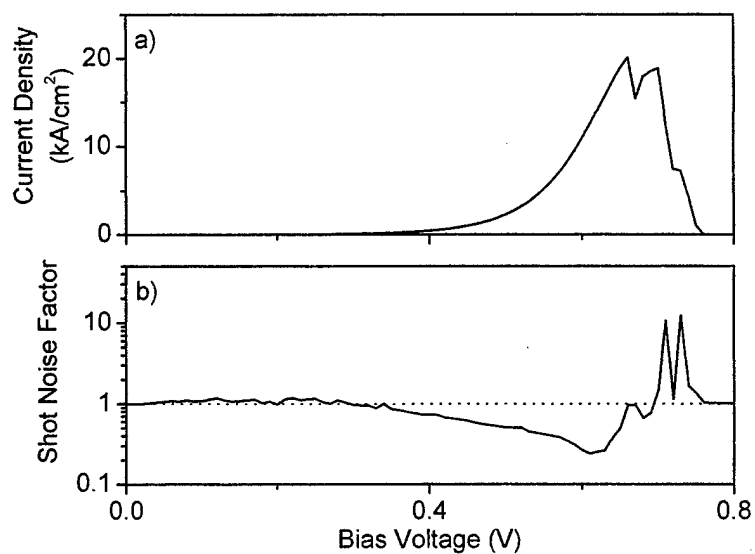


Fig. 18 Structure A3: Triple-well RTD – (a) current density and (b) shot noise factor vs. bias voltage. A minimum shot noise factor of 0.24 is achieved. The shot noise factor curve exhibits three peaks as expected at 0.67 V, 0.73 V and 0.75 V. The small undulations in the shot noise factor are caused by numerical truncation.

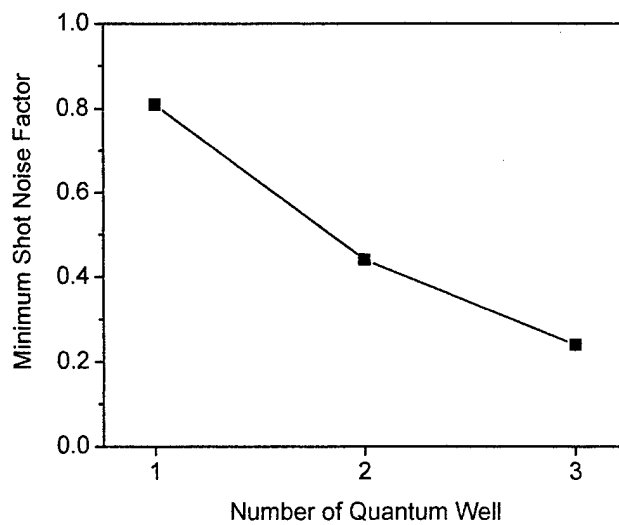


Fig. 19 Minimum shot noise factor vs. well number in simulated structures A1, A2, and A3.

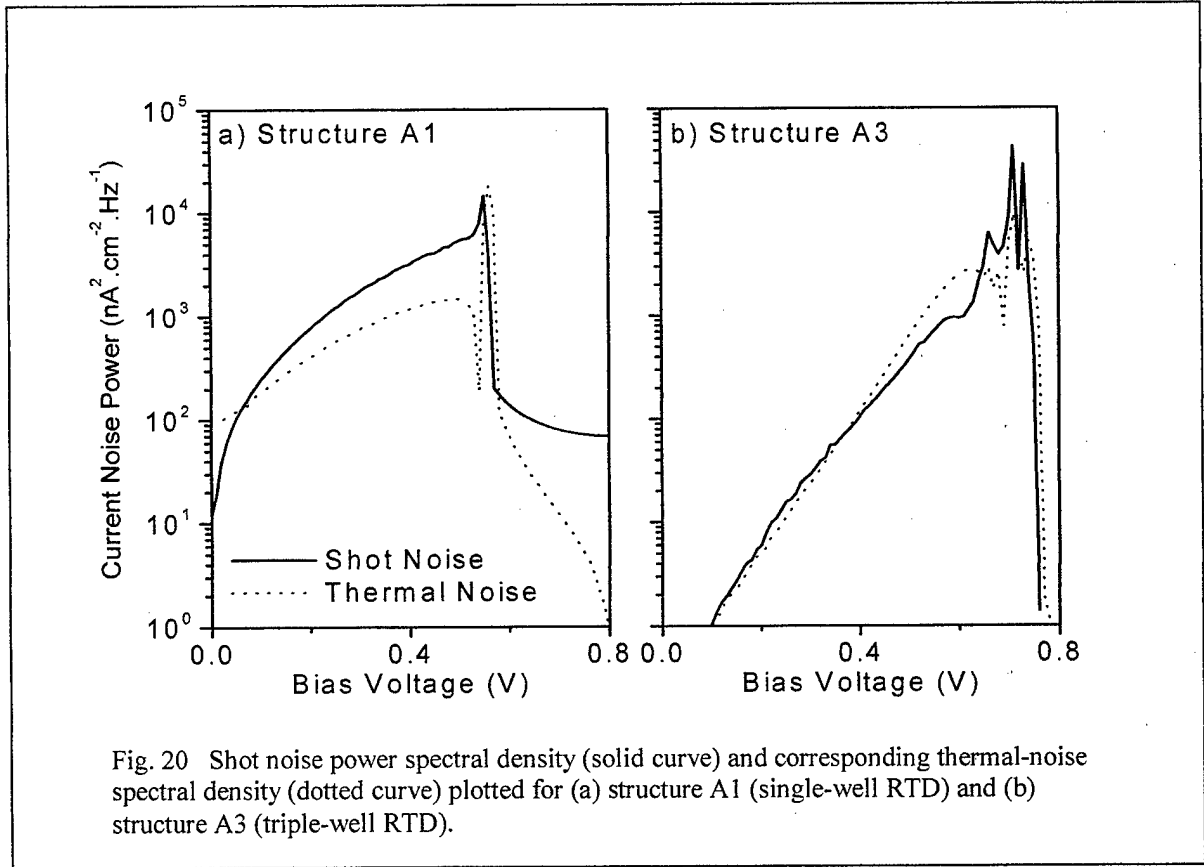
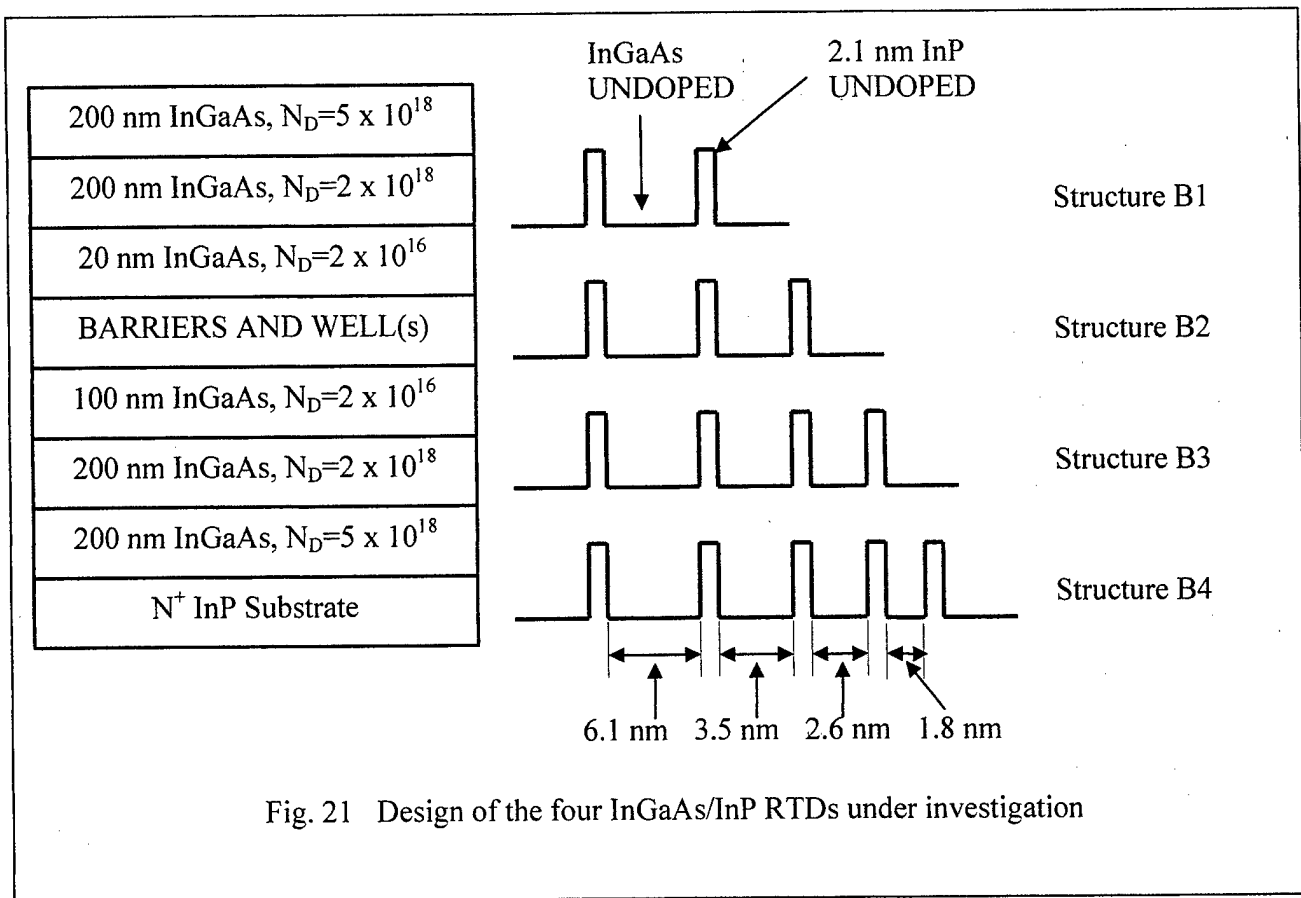


Fig. 20 Shot noise power spectral density (solid curve) and corresponding thermal-noise spectral density (dotted curve) plotted for (a) structure A1 (single-well RTD) and (b) structure A3 (triple-well RTD).

From Figs. 16, 17, and 18, the thermal noise at voltages just below the NDR region increases with well number because the slope of the I-V curve gets steeper. For structure A1 the thermal noise is practically negligible, whereas for the triple-well structure A3 the thermal noise actually becomes dominant (Fig. 20). Hence, from a quantitative standpoint, the present simulation results indicate that multiple-well resonant tunneling structures may not have a better overall noise performance than their single-well counterpart. However we still think the simulation results are promising because the present model does not account for scattering in the well(s). Inclusion of scattering would broaden the overall transmission function and thereby smear out the sharp increase in the current that occurs when the transmission function enters the Fermi sea on the emitter side. Hence, both the conductance G and the thermal noise contribution to the noise spectral density would decrease. On the other hand, we believe the shot noise reduction effect would not be significantly affected by scattering. By our model, it is essentially an electrostatic effect, dependent primarily on the amount of charge stored in the well(s) and not on the nature of the tunneling process. This is supported by previous experimental measurement of significant shot noise reduction in single and double-well RTDs in which sequential tunneling was dominant [32]-[34].

The investigation of shot noise in multiple-well InGaAs/AlAs structures could not be extended to quintuple-barrier structures due to numerical difficulties.



2.5.2. InGaAs/InP Structures

The same kinds of simulations have been carried out for $\text{In}_{0.53}\text{Ga}_{0.47}\text{As}/\text{InP}$ structures. InP is a less promising material as a potential barrier to electrons than AlAs because the conduction band offset with lattice-matched InGaAs is only 0.263 eV (versus 1.2 eV with AlAs). This leads to smaller peak-to-valley current ratios, but it has the advantage of being much easier to grow. Although no experimental data are available to validate the model for this material system, the results are interesting. A standard single-well RTD and three graded quantum well structures have been investigated. The design of these structures is shown in Fig. 21 and the simulation results are presented in Figs. 22 and 23. From Fig. 24, the same decrease of the minimum shot noise factor with the number of well is obtained as in Fig. 19. However it seems the curve flattens at about four wells. This is probably due to the fact that the potential barrier is not very high for this material system, so that electrons are able to transit elastically over the top of the last barrier of the biased quadruple-well structure. Quantization of electrons in the fourth well is thus reduced, and the presence of this well does not assist the shot noise reduction effect.

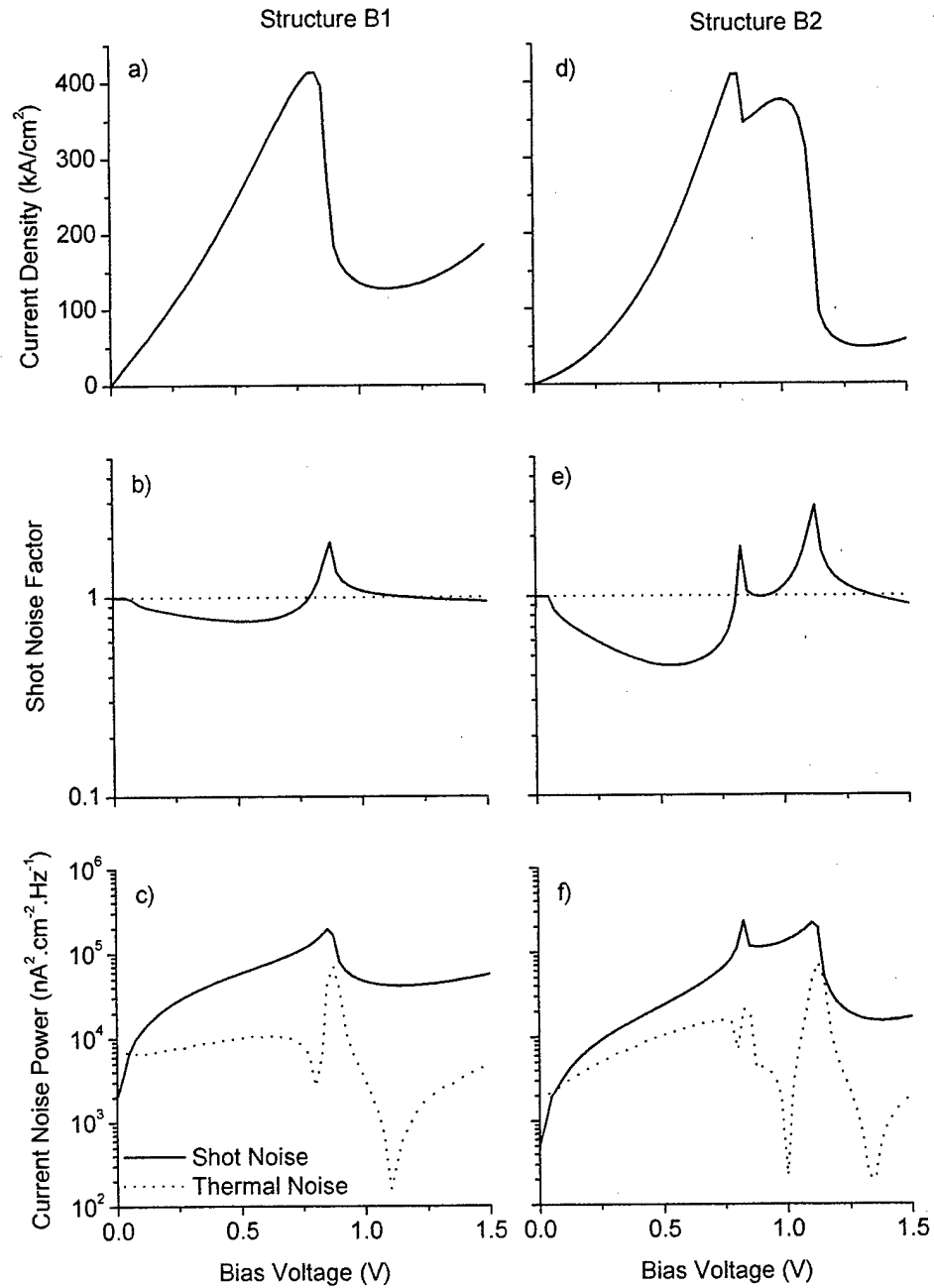


Fig. 22 Simulation results for structure B1 ((a), (b) and (c)) and structure B2 ((d), (e) and (f))

2.6. Promising Application

From a practical standpoint, the main advantages of multiple-well resonant tunneling diodes may be their low noise characteristics, as analyzed here, and their

broader NDR region than in single-well devices [31]. A rough estimate of the speed can be obtained by calculating the differential capacitance $C = \partial Q / \partial V$ and resistance $R = \partial V / \partial I$ of the device. The maximum frequency of operation around a given bias can then be estimated by:

$$f_{\max} = \frac{1}{2\pi RC}$$

For the triple-well InGaAs/AlAs structure (structure A3, Fig. 18) at the bias for which the shot noise reduction effect is maximum (0.61 V), computation and differentiation of the total negative charge and differentiation of Fig. 18 leads $C \approx 8.0 \times 10^{-8} \text{ F-cm}^{-2}$ and $R = 6.2 \times 10^{-6} \Omega\text{-cm}^2$, corresponding to an RC time constant of 0.5 ps and a maximum frequency $(2\pi RC)^{-1}$ of 320 GHz. Although this is less than the f_{\max} of the best single-well RTDs, it is still in the competitive arena of modern high-speed devices.

The main application envisioned for the multiple-well resonant tunneling structure is the fabrication of a low noise microwave vertical field-effect transistor using the tunneling structure as the channel of the device. Many groups reported the fabrication of resonant tunneling transistors using different techniques [35]-[40]. The most common design is to add a Schottky gate on the side of the resonant tunneling diode. Its principle of operation is to control the tunneling current by modulation of the depletion region formed around the gate. The extent of this depletion region determines the effective area through which electrons can tunnel. Using a triple-well structure for the channel of the device would allow achieving a better noise figure without deteriorating its transconductance. However the scaling of the tunneling current with the effective area of the device is not perfect, especially at room temperature. Many challenges in the fabrication of resonant tunneling transistor have to be overcome before it is a practical device.

3. Resonant-Plasmon-Mediated Nanostructures

Besides quantum-well heterostructures, another interesting way to get charge storage in semiconductors is embedded metallic or semimetallic layers, or similar nanoparticles. One of the more interesting means of forming bulk metallic defects in GaAs has been low-temperature growth LTG ($\sim 200^\circ\text{C}$) whereby excess As atoms are incorporated uniformly in the material during molecular-beam epitaxy (MBE) [41]. By an annealing step, many of the excess As atoms precipitate, creating embedded semimetallic nanoparticles but maintaining high crystallinity in the GaAs. In addition, As-related defects capture most of the free carriers, increasing the room-temperature dark resistivity well above the values of normal undoped GaAs.

Table I. ErAs:GaAs Material Characteristics		
Sample	ErAs layer thickness (monolayer)	Fill Fraction (%)
1	0.8	0.56
2	1.2	0.85
3	1.6	1.13

More recently, the useful characteristics of the LTG-GaAs have been obtained at normal growth temperature (535°C) by incorporation of ErAs during the growth [42]. Like excess As in LTG GaAs, the ErAs self-assembles into nanometer-scale semimetallic particles that accumulate excess carriers and act as fast recombination centers. The ErAs approach offers better control over the transport characteristics (e.g., the photocarrier lifetime) of the material. Fortunately, during the course of the present project the group of Prof. Art Gossard at the University of California, Santa Barbara, made various samples of ErAs:GaAs available. In addition, they prepared samples of ErSb:GaSb – a more recent nanoparticle materials system with even better materials characteristics than the ErAs:GaAs. Samples from both materials systems were studied optically and electrically.

3.1 Optical Characterization of ErAs:GaAs

In this research we carried out the first known measurements of the optical attenuation of the ErAs:GaAs material at photon energies well below the GaAs band edge. Three samples were measured at room temperature, each consisting of 30 layers of thin ErAs separated from each other by 40 nm of undoped GaAs. As listed in Table I, the samples differed only in the thickness of the ErAs layers of 0.8, 1.2, and 1.6 monolayer for samples 1, 2, and 3, respectively. All three were grown by MBE under conditions identical to those described previously except for the growth temperature of 630°C. Studies of the microstructure in samples grown at 535°C show that the ErAs forms nm-sized islands [43] about 3 to 4 ML (0.9 to 1.2 nm) high and about 1 to 2 nm in lateral dimension. They form isolated islands at low ErAs deposition and network-like structures at higher deposition. Unpublished studies of samples grown at 630°C (separate from the samples studied here) show that the deposited ErAs forms isolated islands, which are again about 3 to 4 ML (0.9 to 1.2 nm) high, but now extend over a broad range up to ~10 nm in the lateral dimensions [44]. The island density at a deposition of 1.6 ML is approximately $4 \times 10^{11} \text{ cm}^{-2}$. The changing deposition is expected to mainly affect the island density.

Optical transmission measurements on the three samples were carried out with two instruments: a Shimadzu Model UV-3101PC grating monochromator (PbS detector and tungsten source, 2 cm^{-1} resolution) operating between 0.8 and 2.5 micron, and a Jasco Model 420 Fourier-transform infrared (FTIR) spectrometer (pyroelectric detector, incandescent source, 4 cm^{-1} resolution) operating between 2.5 and 10 μm wavelength. Pieces of samples 1, 2, and 3 were mounted in metal holders and the transmission coefficient was determined by dividing the transmitted spectrum I_t by the incident spectrum I_i as measured by the instruments and recorded in units of absorbance, $A = -\log_{10} (I_t/I_i)$. To separate out attenuation effects in the epitaxial layer from the 500- μm -thick semi-insulating (SI) GaAs substrate below it, the absorbance of a bare SI-GaAs substrate from the same lot was also measured.

Because at all measurement wavelengths there was no evidence of standing waves or other complicating multiple-pass effects, we applied Beer's law in conjunction with single-pass transmission through each semiconductor interface to write $T_{\text{sample}} \equiv I_t/I_i = T_1 T_2 \exp(-\alpha_{\text{epi}} t_{\text{epi}}) \exp(-\alpha_{\text{sub}} t_{\text{sub}})$ where T_1 is the power transmission coefficient through the first (air-epitaxial) interface, T_2 is the transmission through the second (substrate-air)

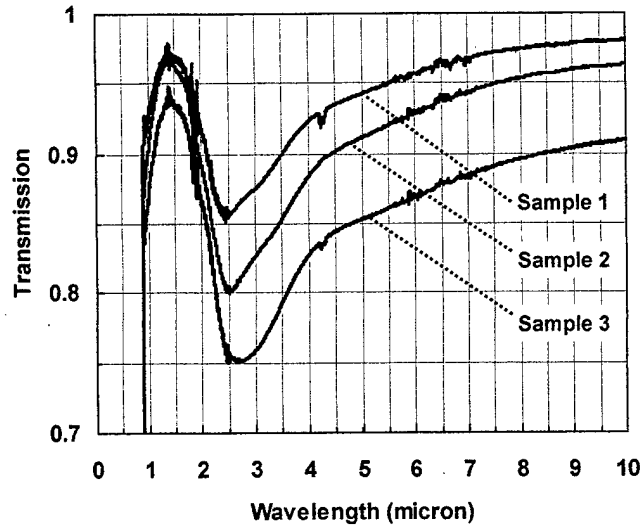


Fig. 23. Normalized intensity transmission coefficient vs. wavelength for three ErAs: GaAs samples at room temperature. The precipitous drop in transmission below 0.9 micron is caused by the fundamental band-gap of GaAs. The weak attenuation features around 1.8, 2.4, and 6.5 μm are caused by H_2O vapor, and the sharper feature at 4.3 micron is attributed to CO_2

interface, $\alpha_{\text{epi}}(t_{\text{epi}})$ is the attenuation coefficient (thickness) of the ErAs-bearing epitaxial layer, and $\alpha_{\text{sub}}(t_{\text{sub}})$ is attenuation coefficient (thickness) of the GaAs substrate. In each sample the substrates were double side polished so that the air-GaAs interfaces were of comparable optical quality and $T_1 \approx T_2 \equiv T$. Hence the ratio of the sample (substrate + epitaxial layer) transmission to the substrate transmission (i.e., the normalized transmission) can be expressed as $T_{\text{sample}}/T_{\text{substrate}} = [T^2 \exp(-\alpha_{\text{epi}} \cdot t_{\text{epi}}) \exp(-\alpha_{\text{sub}} \cdot t_{\text{sub}})] / [T^2 \exp(-\alpha_{\text{sub}} \cdot t_{\text{sub}})] = \exp(-\alpha_{\text{epi}} \cdot t_{\text{epi}})$, and thus $\alpha_{\text{epi}} = -\ln\{T_{\text{sample}}/T_{\text{substrate}}\}/t_{\text{epi}}$

The lack of multiple-pass interference effects in our samples is attributed to the use of incoherent radiation in both spectrometers, and to mounting the samples at the point of an uncollimated beam. Note that the largest transmission measured in the GaAs substrate was approximately 0.55 in good agreement with a single-pass approximation $I_t \approx T^2$ and a T from Fresnel's (normal incidence) equation of $4n_s/(n_s+1)^2 = 0.71$ for $n_s = 3.3$ (accepted value for GaAs in the near-IR at λ s well beyond the band edge). This implies that α_{sub} is negligible in our measurement wavelength range – a plausible result since the present substrates are semi-insulating (very low free carrier absorption).

Plotted in Fig. 23 is the experimental normalized transmission measured through Samples 1-3 between $\lambda = 0.5$ - and 10 μm . To maximize data quality, the signal from 0.5 to 2.5 micron is taken from the grating spectrometer, and the signal from 2.5 to 10.0 micron is taken from the FTIR spectrometer. The dominant features in each spectrum are the precipitous GaAs band edge at ~ 0.85 micron and a broad, asymmetric attenuation feature centered around 2.48, 2.55, and 2.59 micron for Samples 1, 2, and 3, respectively. The depth of the attenuation feature grows continuously between Samples 1 and 3. The three curves also display spurious absorption bands centered around 2.6, and 6.5 microns that are attributed to residual H_2O vapor in the spectrometer, and a sharp feature at 4.3 micron that is attributed to CO_2 .

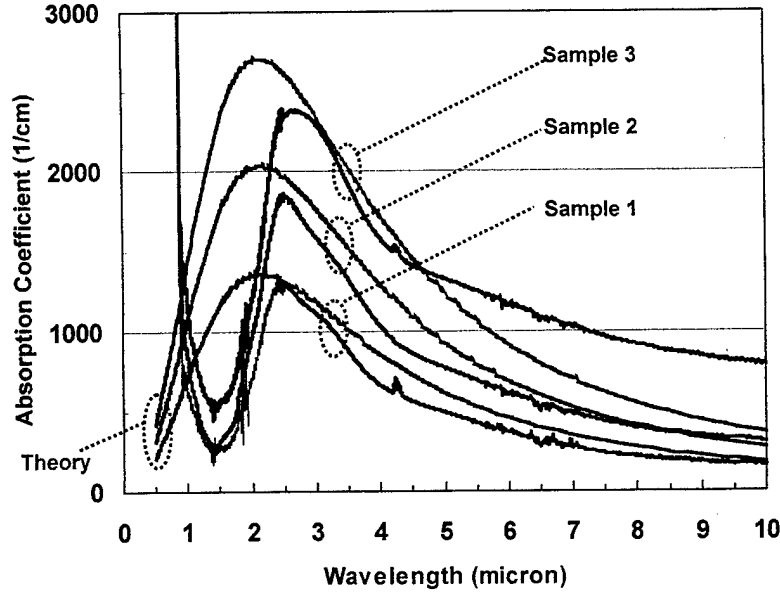


Fig. 24. Plots of experimental attenuation coefficient vs. wavelength for the three ErAs: GaAs samples at room temperature. The attenuation length is assumed to be the entire 1.2- μm epitaxial layer of each sample. Also shown are the theoretical curves fit to experiment according to the Maxwell-Garnett and Drude models described in the text.

Plotted in Fig. 24 is the attenuation coefficient derived from the normalized transmission using the expression given above. Note that our experiments cannot distinguish attenuation by absorption from attenuation by scattering. Since the epitaxial thickness is 1200 nm for each sample, the peak attenuation coefficient of the 2.5-micron attenuation feature is approximately 1300, 1850, and 2380 cm^{-1} for Samples 1, 2, and 3, respectively. The asymmetry of this feature appears clearly as a long-wavelength tail that produces easily measured attenuation, even at $\lambda = 10$ microns. The peak attenuation values are surprisingly high considering that the material presumably responsible for the attenuation, the ErAs layers, constitute only about 1% of the epitaxial volume.

3.2 Modeling of ErAs Nanoparticles: Surface Plasmons

To understand the experimental results we have considered several possible attenuation mechanisms including free-carrier optical effects, quantum-size effects, and photoionization from the ErAs nanoparticles. The most accurate mechanism has been by far the free carrier effects, which are predicted to be very strong because of a surface plasmon (Frohlich) resonance in the ErAs nanoparticles. Our free-carrier optical model treats the ErAs: GaAs epilayer as a composite medium consisting of independent ErAs nanoparticles separated by insulating GaAs. Consistent with previous experiments [45] and theory [46], the ErAs is treated as a semimetal using the Drude model to account for the free-carrier optics. As such, we can write for the dielectric function of the ErAs [47]

$$\epsilon_s = \epsilon_B + \frac{\omega_p^2}{-\omega^2 - i\omega\gamma} \quad (1)$$

where ϵ_B is the (real) background dielectric constant, ω is the circular optical frequency, ω_p is the plasma frequency, and γ ($= 1/\tau$) is the free-carrier scattering frequency and τ is

the scattering time. In the composite medium, the GaAs matrix is expected to modify the dielectric function in a manner that depends critically on the size and shape of the ErAs nanoparticles [48]. In our samples and over the experimental wavelength range, we know that the ErAs particles are much smaller than λ . If we also assume that the ErAs particles occupy a relatively small fraction of the total material volume and are optically independent, we can apply one of the truly venerable theories of optical physics, the Maxwell-Garnett (M-G) formulation. In its general form, the M-G predicts a composite dielectric function of the form

$$\epsilon = \frac{(1-f)\epsilon_M + f\beta\epsilon_S}{1-f+f\beta} \quad (2)$$

where ϵ_M is the dielectric constant of the GaAs matrix, f is the volumetric fill fraction of the ErAs component, and β is a numerical factor that depends on the shape and size of the ErAs nanoparticles. For the special case of spherical particles, the volume dependence vanishes and β reduces to $3\epsilon_M/(\epsilon_S + 2\epsilon_M)$, leading to the expression,

$$\epsilon = \epsilon_M \frac{2\epsilon_M + \epsilon_S + 2f(\epsilon_S - \epsilon_M)}{2\epsilon_M + \epsilon_S - f(\epsilon_S - \epsilon_M)} \quad (3)$$

From lattice-images taken of material similar to that measured here, we know that the ErAs nanoparticles are closer to ellipsoidal in shape than spherical, but we proceed with the spherical assumption because of its great simplicity and utility in providing a first explanation of the experimental results.

To apply Eqns (1) and (3) in the present samples, we must know values for 5 material-dependent quantities. The volumetric fraction is known accurately in each sample from MBE thickness measurements (RHEED oscillations) and is listed in Table I. The GaAs matrix has a dielectric constant that is slowly varying over the experimental range with an average value of $\epsilon_M \approx 10.9$. To get ω_p , γ , and ϵ_B in the nanoparticles, we must rely on theoretical estimation since the semimetallic nature of ErAs means that electrons and holes will both contribute to any transport effect (including plasma excitations), and contribution of each carrier type to the plasma frequency will depend on the detailed band structure. It is known that ErAs has a rocksalt band structure so that the electrons reside in ellipsoidal valleys characterized by a longitudinal and transverse effective masses, m_L and m_T , respectively. The holes reside in three warped-sphere bands, the light-hole, heavy-hole, and split-off bands having effective masses m_{LH} , m_{HH} , and m_{SO} , respectively. Fortunately a great deal of experimental work based on the Shubnikov-de-Haas effect coupled with band structure calculations has also produced the concentrations of each carrier type, as listed in Table II. Given these quantities and given the applicability of the semiclassical model of transport of independent carriers,⁷ an interesting exercise in deductive reasoning is to show that the plasma frequency of a many-carrier solid is given by [49] (in MKS units),

$$\omega^2 = \frac{e^2}{\epsilon_0} \frac{\sum_{i=1}^N (\rho_i \cdot \prod_{j \neq i}^N m_j)}{\prod_{i=1}^N m_i} \equiv \frac{e^2}{\epsilon_0} \left\langle \frac{\rho}{m} \right\rangle \quad (4)$$

where e is the electron charge, ϵ_0 is the vacuum permittivity, N is the number of relevant bands, and the symbol $\langle \rho/m \rangle$ symbolizes the averaging process defined by (4) over the densities and effective masses. For example, in the four-band model of ErAs we find:

$$\omega_p^2 = \frac{e^2}{\epsilon_0} \left[\frac{\rho_e m_{lh} m_{hh} m_{so} + \rho_{lh} m_e m_{hh} m_{so} + \rho_{hh} m_e m_{lh} m_{so} + \rho_{so} m_e m_{lh} m_{hh}}{m_e m_{lh} m_{hh} m_{so}} \right] \quad (5)$$

Given the material characteristics in Table II this results in a linear plasma frequency ($\omega_p/2\pi$) of 6.7×10^{14} Hz, corresponding to a plasma (cutoff) wavelength of $0.45 \mu\text{m}$. This is considerably longer than the plasma cut-off in most metals since the total carrier concentration in the ErAs ($8.3 \times 10^{20} \text{ cm}^{-3}$) is so much lower (e.g., in copper $\rho = 8.4 \times 10^{22} \text{ cm}^{-3}$).

The final two quantities in the model are the least certain, but are also not as crucial to our interpretation of the experimental data. The scattering frequency is a complicated function of particle size and shape, but simplifies to $\gamma = \gamma_{\text{bulk}} + 3\langle v_F \rangle/2d$ for spherical particles, where γ_{bulk} is the bulk scattering frequency, $\langle v_F \rangle$ is the average Fermi velocity, and d is the diameter of the sphere [50]. γ_{bulk} can be estimated from measurements made on the conductivity of continuous ErAs films on GaAs at room temperature, $\sigma \approx 1.5 \times 10^4 \text{ } \Omega\text{-cm}$ [51]. The bulk scattering can then be estimated through the following variation of (4),

$$\gamma = \frac{e^2}{\sigma} \left\langle \frac{\rho}{m} \right\rangle \quad (6)$$

where γ is assumed to be independent of carrier type. Substitution of the experimental conductivity along with the value $e^2 \langle \rho/m \rangle = 1.58 \times 10^{20}$, yields $\gamma_{\text{bulk}} = 1.05 \times 10^{14} \text{ s}^{-1}$, or $\tau_{\text{bulk}} = 9.9 \text{ fs}$ - a reasonable result since it is so close to the Drudian scattering time in common metals (e.g., $\tau \approx 10 \text{ fs}$ in Al). To get the surface-scattering contribution, we write the Fermi velocity in each band according to the well-known expression

$$v_{F,i} = (\hbar / m_i) (3\pi^2 \rho_i)^{1/3} \text{ and calculate an average by } \langle v_F \rangle = \frac{\sum_{i=1}^N (\rho_i v_{F,i})}{\sum_{i=1}^N \rho_i}.$$

This leads to the result for ErAs of $\langle v_F \rangle = 1.14 \times 10^6 \text{ m/s}$ - a value comparable to that in common metals (e.g., v_F in Al = $2.02 \times 10^6 \text{ m/s}$), in spite of the much lower concentration of free carriers in ErAs. For the ErAs nanoparticles previously imaged by TEM methods the size of the particles is in the range of 1 to 2 nm. When combined with the above value of $\langle v_F \rangle$, the estimated range of γ is 1.7×10^{15} to $8.5 \times 10^{14} \text{ s}^{-1}$ ($\tau = 5.8 \times 10^{-16} \text{ s}$ to $1.2 \times 10^{-15} \text{ s}$), well below the bulk value. Because we do not yet know the exact distribution of sizes and shapes of the nanoparticles in the present samples, the diameter will be treated as a fitting parameter and compared with the above range for credibility.

3.3 Surface plasmon effect on optical transmission

The final physical quantity in the model is ϵ_B - the background dielectric constant associated with the core electrons. As in many metals this quantity is hard to measure and calculate, so we will assume it to be 1.0. In the wavelength range of measurement, the dependence on ϵ_B is weak anyway because both the real and imaginary part of the ϵ is

determined by the large GaAs background ϵ_M and plasma effects. Given the 5 quantities and the dielectric function of (3), we can calculate the attenuation and propagation coefficient, α and β , respectively, from classical electromagnetics,

$$\alpha, \beta = (2\omega/c) \{ (\mu' \epsilon'/2) \{ [1 + (\epsilon''/\epsilon')^2]^{1/2} - 1 \} \}^{1/2}, \quad (7)$$

where c is the speed of light in vacuum ϵ' (ϵ'') are the real and imaginary parts of the M-G dielectric function of (3), and μ' is the relative magnetic permeability [52]. Although ErAs is known to have a large positive μ' owing to unfilled inner-shell paramagnetism, such effects are almost certainly relaxed at the present wavelengths, so that we can assume $\mu'=1$. Note that we call this an *absorption* rather than attenuation coefficient since the M-G theory treats the entire epitaxial layer as a uniform composite medium. Backscatter is also accounted for by this formalism but shows up through modification of β (i.e., the real part of the refractive index) and a modification of the reflection coefficient via the Fresnel equations.

Fig. 24 shows the computed value of the *intensity* attenuation constant 2α according to the quantities calculated for each of the three ErAs:GaAs samples. The only fitting parameter – the diameter of the spherical particles, d – is set equal to 1.2 nm. Remarkably, the theoretical curves display very similar behavior to the experimental ones. Each theoretical curve shows an asymmetric resonance peak with a long-wavelength tail that has significant absorption even at $\lambda = 10 \mu\text{m}$. The absorption increases monotonically in peak strength with increasing ErAs fill fraction, although the theoretical peak wavelength for each sample – $\lambda_p = 2.1 \mu\text{m}$ – is somewhat shorter than the experimental peaks. This disagreement in peak wavelength causes a significant discrepancy between experimental attenuation and theoretical absorption on the short-wavelength side. Note, however, that the slope of the theoretical and experimental curves is nearly the same. Note also that the fit value of $d = 1.2 \text{ nm}$ is in the range of expected nanoparticle thickness (0.9 to 1.2 nm) in the present samples, but is well below the expected lateral dimension.

To further support the absorptive model we also computed the M-G intensity reflection coefficient R according to (3) and (7) and the Fresnel equation, $R = |(\epsilon^{1/2} - 1)/(\epsilon^{1/2} + 1)|^2$. We find no resonance in R around $2.5 \mu\text{m}$, although there is a weak variation vs λ consistent with the Drude model. To explain the discrepancies between model and experiment, we note that a more refined analysis would represent the nanoparticles not as perfect spheres but as ellipsoids or, possibly, spheroids. In either case, the M-G and full-wave scattering theories would both predict the resonant absorption to shift to longer wavelengths relative to the peak of the spherical-particle curve [48]. Because an optical sum rule applies to the free-carrier optics, the peak absorption would also diminish relative to that of the spherical-particle model, and thus broaden the overall signature – more consistent with experimental results.

Given the qualitative success of the model, it is compelling to elucidate the nano-optics behind the effect. It is well known that metal particles dispersed at low fill fraction in an insulating host can display resonant attenuation below the bulk plasma frequency associated with normal electromagnetic modes of the particle. When the normal mode is quantized, these become the so-called surface *plasmons*. Remarkably, the fundamental mode can be predicted from the M-G theory in the limit of very small fill

fraction. In this case (3) displays a pole in the dielectric function at the frequency where $\epsilon_S \approx -2\epsilon_M$ a condition credited to Frohlich [53]. For the Drude model of free-carrier optics, this condition becomes simple to interpret in the range $\gamma \ll \omega$. Then from (1), the frequency that satisfies $\epsilon_S \approx -2\epsilon_M$ is simply $\omega = \omega_p/(\epsilon_B + 2\epsilon_M)^{1/2} \equiv \omega_F$ [54], often called the Frohlich resonant frequency. In the present samples with $\omega_p = 4.2 \times 10^{15}$ Hz, $\lambda_p = 0.45 \mu\text{m}$, $\epsilon_M = 10.9$ and $\epsilon_B \approx 1.0$, we find $\omega_F = 8.8 \times 10^{14}$ Hz and $\lambda_F = 2.1 \mu\text{m}$, in good agreement with the peak of the model attenuation curves.

Note, however, that in the present samples we do not satisfy $\gamma \ll \omega$. Rather, because of the small size of the nanoparticles and the associated surface scattering, our estimation of γ yields a value of $9.6 \times 10^{14} \text{ s}^{-1}$ – slightly larger than ω_F . Hence, the simple interpretation given above is not strictly valid. Nevertheless, the model resonance persists and its peak remains near $\lambda_F = 2.1 \mu\text{m}$. Although it is not simple to prove this mathematically from (1), (3), and (7), it can be argued from the following classical viewpoint. The normal mode that gives rise to the surface plasmon and Frohlich resonance is a result of classical electromagnetics and the Drude model. In other words, it is just one form of a Lorentzian atomic resonator with zero resonance frequency. As such, when the damping factor (γ in our case) increases, the resonance broadens and weakens but in a gradual fashion, so the peak persists and the peak frequency remains approximately constant.

It is important to contrast our results with the previous work by Nolte et al. who sought to observe Frohlich resonances in metal precipitates in GaAs and AlGaAs samples, particularly As in low-temperature-grown GaAs [55,56]. First, it is possible that their measurements, which were only taken out to $1.5 \mu\text{m}$, did not go far enough in wavelength to observe a resonance in the As:GaAs samples. And the presence of standing waves in the AlGaAs layers of the As:AlGaAs samples would, in our experience, make it very difficult to observe the resonances at the attenuation strength observed in our samples. Second, it is quite possible that our ErAs nanoparticles are much more monodisperse in size and shape than the As precipitates in the low-temperature-grown samples. More lattice-imaging experiments will be required to prove this. But if true, we anticipate that because of the strength of the surface-plasmon resonance, ErAs nanoparticles will offer a new means of engineering the optical properties of GaAs and InGaAs at near-infrared wavelengths where widespread technological development continues for optical-fiber telecommunications and other applications.

Table II. Band Properties of ErAs ⁶		
Band	Carrier Concentration (cm^{-3})	Effective Mass ($\times m_e$)
Electron	4.14E+20	0.21
Light Hole	1.19E+20	0.28
Heavy Hole	2.93E+20	0.46
Split-Off	2.00E+18	0.15

Conclusion

Through this research, a formalism that enables the study of the noise properties of multiple-well resonant tunneling diodes has been developed. The shot noise reduction effect is modeled as the result of the electrostatic repulsion encountered by the injected carriers due to the charge stored in the quantum well(s). Simulation results are compared successfully to experimental results, and then carried out for the first time on multiple-well resonant tunneling structures. It appears that multiple-well structures show superior noise properties, i.e., a greater shot noise reduction effect, than their single-well counterpart. These simulation results must be confirmed experimentally but are already promising for the use of multiple- quantum-well structures in new low-noise devices and circuits.

In the spirit of "Fermi-electronics", this research has also spawned the discovery of very strong plasmon-mediated optical absorption in a semimetal-semiconductor composite: ErAs:GaAs. Strong absorption signatures have been observed just below the GaAs band-edge, and have been explained theoretically in terms of a surface plasmon resonance. This research paves the way for a class of optically- and (perhaps) electrically triggered switches in which the gating function is carried out by *resonant* plasmons. Although similar in spirit to plasma-electronic devices recently studied by M. Shur et al., *resonant* plasmon coupling is much stronger so that the devices can have much higher electrical or optoelectronic gain.

References

1. A van der Ziel, Noise in Solid State Devices and Circuits. Wiley, New York, 1986, chapter 3.
2. E. R. Brown, "Analytic Model of Shot Noise in Double-Barrier Resonant Tunneling Diodes", IEEE Trans. Electron Devices, vol. 39, pp. 2686, 1992.
3. J. P. SUN and al, "Resonant Tunneling Diodes: Models and Properties", Proceedings of the IEEE, vol. 86, pp. 641, 1998
4. E. R. Brown and al, "A Quasioptical Resonant Tunneling Diode Oscillator Operating above 200 GHz", IEEE Trans. On Microwave Theory and Techniques, vol. 41, pp. 720, 1993
5. E. R. Brown and al, "Suppressed gate current in a superlattice-insulated-gate field-effect transistor on InP", Appl. Phys. Lett., vol. 66, pp. 2352, 1995
6. T. Wei and S. Stapleton, "Effect of spacer layers on capacitance of resonant tunneling diodes", J. Appl. Phys., vol. 76, pp. 1287, 1994
7. R. C. Bowen and al, "Quantitative Simulation of a Resonant Tunneling Diode", J. Appl. Phys., vol. 81, pp. 3207, 1997
8. J. N. Schulman and T. C. McGill, "Complex band structure and superlattice states", Phys. Rev. B, vol. 23, pp. 4149, 1981
9. H. Asai and Y. Kawamura, Phys. Rev. B, vol. 43, pp. 4748, 1991
10. J. H. Luscombe, "Current Issues in Nanoelectronic Modeling", Nanotechnology, vol. 4, pp. 1, 1993.
11. Y. Ando and T. Itoh, "Calculation of transmission tunneling current across arbitrary potential barriers", J. Appl. Phys., vol. 61, 1987
12. W. Pötz, "Self-consistent model of transport in quantum well tunneling structures", J. Appl. Phys., vol. 66, pp. 2458, 1989
13. R. Tsu and L. Esaki, "Tunneling in a Finite Superlattice", Appl. Phys. Lett., vol. 22, pp. 562, 1973.

14. S. Collins, D. Lowe and J. R. Barker, "Resonant tunneling in heterostructures: Numerical simulation and qualitative analysis of the current density", *J. Appl. Phys.*, vol. 63, pp. 142, 1988
15. M. Cahay and *al*, "Importance of space-charge effects in resonant tunneling devices", *Appl. Phys. Lett.*, vol. 50, pp. 612, 1987
16. G. Klimeck and *al*, "Quantum device simulation with generalized tunneling formula", *Appl. Phys. Lett.*, vol. 67, 1995
17. F. Chevoir and B. Vinter, "Scattering-assisted tunneling in double-barrier diodes: Scattering rates and valley current", *Phys. Rev. B*, vol. 47, pp. 7260, 1993
18. G. Dahlquist and Å. Björk, *Numerical Methods*, Prentice-Hall, New Jersey, 1974
19. K. F. Brennan, "Self-consistent analysis of resonant tunneling in a two-barrier-one-well microstructure", *J. Appl. Phys.*, vol. 62, pp. 2392, 1987
20. M. A. Alam and A. N. Khondker, "An efficient self-consistent model for resonant tunneling structures", *J. Appl. Phys.*, vol. 68, pp. 6501, 1990
21. D. G. Anderson, "Iterative Procedure for Nonlinear Integral Equations", *ACM Journal*, vol. 12, pp. 547, 1965.
22. R. Guerrieri and *al*, "Vectorial Convergence-Acceleration Techniques in Semiconductor Device Analysis"
23. F. N. H. Robinson, "Noise and Fluctuations in Electronic Devices and Circuits", Oxford, UK: Clarendon, 1974, sec. 5.4
24. E. R. Brown, T. C. L. G. Sollner and W. D. Goodhue, "Noise properties of quantum well structures", *Solid State Research Report*, Lexington, MA: MIT Lincoln Lab., 1986, no. 1, pp. 37
25. Y. P. Li and *al*, "Noise characteristics of double-barrier resonant tunneling structures below 10 kHz", *Phys. Rev. B*, vol. 41, pp. 8388, 1990
26. J. Han and F. S. Barnes, "A theory of shot noise in quantum wells and applications in resonant tunneling heterojunction bipolar transistors", *IEEE Trans. Electron Devices*, vol. 38, pp. 237, 1991
27. E. R. Brown and *al*, "Low shot noise in high-speed resonant tunneling diodes", *IEEE trans. Electron Devices*, vol. 38, pp. 2716, 1991
28. D. Landheer and *al*, "Tunneling through AlAs barriers: Γ -X transfer current", *Appl. Phys. Lett.*, vol. 54, pp. 1784, 1989
29. Peng Cheng and *al*, "The X-valley transport in GaAs / AlAs triple barrier structures", *J. Appl. Phys.*, vol. 65, pp. 5199, 1989
30. C. J. Summers and K. F. Brennan, "Variably spaced superlattice energy filter, a new device design concept for high-energy electron injection", *Appl. Phys. Lett.*, vol. 48, pp. 806, 1986
31. E. R. Brown and *al*, "Resonant tunneling through mixed quasibound states in a triple-well structure", *Appl. Phys. Lett.*, vol. 62, pp. 3016, 1993
32. G. Iannaccone and *al*, "Simulation and Measurement of Shot Noise in Resonant Tunneling Structures", *Analog IC and Signal Processing*, vol. 24, pp. 73, 2000
33. H. C. Liu and *al*, "Shot noise suppression in resonant tunneling", *Phys. Rev. B*, vol. 51, pp. 5116, 1995
34. S.-T. Yau and *al*, "Shot noise of sequential tunneling in a triple-barrier resonant-tunneling diode", *Phys. Rev. B*, vol. 55, pp. 12880, 1997
35. P. H. Beton and *al*, "Edge effects in a gated submicron resonant tunneling diode", *Appl. Phys. Lett.*, vol. 60, pp. 2508, 1992
36. P. Gueret and *al*, "Confinement and Single-Electron Tunneling in Schottky-Gated, Laterally Squeezed Double-Barrier Quantum-Well Heterostructures", *Phys. Rev. Lett.*, vol. 68, pp. 1896, 1992
37. C. J. Goodings and *al*, "Variable-area resonant tunneling diodes using implanted in-plane gates", *J. Appl. Phys.*, vol. 76, pp. 1276, 1994

38. V. R. Kolagunta and *al*, "Self-aligned sidewall gated resonant tunneling transistors", Appl. Phys. Lett., vol. 69, pp. 374, 1996
 39. L.-E. Wernersson and *al*, "Lateral current-constriction in vertical devices using openings in buried lattices of metallic discs", Appl. Phys. Lett., vol. 71, pp. 2803, 1997
 40. B. Gustafson and *al*, "Lateral current confinement in selectively grown resonant tunneling transistor with an embedded gate", Physica E, vol. 7, pp. 819, 2000
-
41. F.W. Smith, A.R. Calawa, C.L. Chen, M.J. Manfra, and L.J. Mahoney, IEEE Electron Device Lett. Vol. 9, p. 77 (1988).
 42. C. Kadow, S.B. Fleischer, J.P. Ibbetson, J.E. Bowers, A.C. Gossard, J.W. Dong, and C.J. Palmstrom, Appl. Phys. Lett. Vol., 75, pp. 3548-3550 (1999).
 43. C. Kadow, J.A. Johnson, K. Kolstad, J.P. Ibbetson, and A.C. Gossard, J. Vac. Sci. Tech. B, vol. 18, no. 4, p. 2197 (2000).
 44. C. Kadow, University of California, Santa Barbara, private communication.
 45. S.J. Allen Jr., N. Tabatabaie, C.J. Palmstrom, G.W. Hull, T. Sands, F. DeRosa, H.L. Gilchrist, and K.C. Garrison, Phys. Rev. Lett. 62, 2309 (1989).
 46. W.R.L. Lambrecht, B. Segall, A.G. Petukhov, R. Bogaerts, and F. Herlach, Phys. Rev. B, vol. 55, 9239 (1997).
 47. Ashcroft and Mermin, Solid State Physics (Holt, Rinehart, and Winston, New York, 1976).
 48. C.F. Bohren and D.R. Huffman, "Absorption and Scattering of Light by Small Particles," (Wiley, New York, 1983).
 49. E.R. Brown, unpublished.
 50. U. Kriebel, "Electronic properties of small silver particles: the optical constants and their temperature dependence," J. Phys. F., vol. 4, pp. 999-1014.
 51. J. Ralston, H. Ennen, P. Wennekers, P. Hiesinger, N. Herres, J. Schneider, H.D. Muller, W. Rothmund, F. Fuchs, J. Schmalzlin, and K. Thonke, J. Electronic Materials, vol. 19, no. 6 (1990).
 52. F. Ulaby, Fundamentals of Applied Electromagnetics, (Prentice Hall, Upper Saddle River, NJ, 1999 Edition), Sec. 7-4.
 53. H. Frohlich, Theory of Dielectrics (Oxford University Press, London, 1949).
 54. Note that when $\epsilon_B = \epsilon_M = 1$, ω_F reduces to $\omega_p/(3)^{1/2}$, the well-known ground-state resonance frequency for a spherical metal particle in vacuum, which should not be confused with the resonance $\omega_p/(2)^{1/2}$ for a slab geometry (see Ref. 7, Chapter 1, Problem 5).
 55. D. D. Nolte, J. Appl. Phys. Vol. 76, p. 3740 (1994).
 56. D. Crouse, D.D. Nolte, J.C.P. Chang, and M.R. Melloch, J. Appl. Phys., vol. 81, p. 7981 (1997).

**LISTING OF PUBLICATIONS AND TECHNICAL REPORTS SUPPORTED
UNDER GRANT DAAD19-99-1-0296**

A. PUBLICATIONS

1. "Shot Noise Reduction Effect in Multiple Quantum Well Resonant Tunneling Diodes," Pouyet, V. and Brown, E.R. IEEE Trans. On Electron Dev., vol. 50, no. 4, pp 1063-1068 (2003).
2. "Evidence for a Strong Surface-Plasmon Resonance on ErAs Nanoparticles in GaAs," E. R. Brown, A. Bacher, D. Driscoll, M. Hanson, C. Kadow, and A. C. Gossard, Phys. Rev. Lett., vol. 90, 077403 (2003).

B. TECHNICAL REPORTS

1. Annual Reports: 1999, 2000, 2001, 2002
2. Thesis titled: Shot Noise Reduction Effect in Multiple Quantum Well Resonant Tunneling Diodes

LISTING OF SCIENTIFIC PERSONNEL EARNING ADVANCED DEGREES

1. **Name:** Vincent Pouyet
Degree awarded: M.S. Electrical Engineering
Year Awarded: 2003